DESIGN AND CONTROL OF A STANDING-WAVE THERMOACOUSTIC REFRIGERATOR

by

Timothy S. Ryan

B.S. in Mechanical Engineering, University of Pittsburgh, 2006

Submitted to the Graduate Faculty of

The Swanson School of Engineering in partial fulfillment

of the requirements for the degree of

Master of Science in Mechanical Engineering

University of Pittsburgh

2009

UNIVERSITY OF PITTSBURGH

SWANSON SCHOOL OF ENGINEERING

This thesis was presented

by

Timothy S. Ryan

It was defended on

November 30, 2009

and approved by

Dr. Jeffrey S. Vipperman, Associate Professor, Department of Mechanical Engineering and Materials Science

Dr. William W. Clark, Professor, Department of Mechanical Engineering and Materials Science

Dr. Laura A. Schaefer, Associate Professor, Department of Mechanical Engineering and Materials Science

Thesis Advisor: Dr. Jeffrey S. Vipperman, Associate Professor, Department of Mechanical Engineering and Materials Science

DESIGN AND CONTROL OF A STANDING-WAVE THERMOACOUSTIC REFRIGERATOR

Timothy S. Ryan, M.S.

University of Pittsburgh, 2009

A thermoacoustic refrigerator was designed using a dimensionless parameter approach. Some basic insight into thermoacoustic design principles was obtained. The resulting device was used as a test bed for three different control schemes. The first was a phase-locked loop, which is the control method most often used in the literature; the second controller utilized a gradient ascent algorithm to track the operating frequency of maximum acoustic pressure; and the third utilized the same gradient ascent architecture to track the operating frequency corresponding to maximum acoustic power transfer to the resonator. The three controllers, tracking different parameters associated with a strong thermoacoustic effect, were compared in simulations and experiments. Difficulties in collecting data for the power controller resulted in unreliable data. Therefore, the power controller was not compared quantitatively with the other two. The PLL performed best in terms of thermoacoustic efficiency, but the acoustic pressure controller was able to produce more cooling power and converted electrical power to cooling power more efficiently due to the amplitude of the input voltage to the driver being held constant. The major short-coming of the gradient ascent approach was the relatively long convergence time. However, convergence time is not always relevant to refrigerator operation. The maximum acoustic pressure control scheme was determined to be the best controller considered because it has fewer sensors than the other two controllers, involves less computational effort than the power controller, and yielded better electrothermal performance than the PLL.

TABLE OF CONTENTS

LIST OF TABLES

LIST OF FIGURES

1.0 INTRODUCTION

1.1 A HISTORY OF THERMOACOUSTICS

Thermoacoustics, in its most general sense, is the study of the interaction between heat and sound. The term has lately become narrower in its meaning so that it refers mostly to the field as applied to heat engines and refrigerators. Thermoacoustics is by no means a new field, but many of the major developments have happened fairly recently. As with many fields, thermoacoustics began as an anecdotal curiosity, but after a fairly long period with little development, a resurgence of interest has led to many advances in theory and experimental methods.

Evidence of thermoacoustic phenomena dates back centuries to when glass blowers first noticed that a hot bulb at the end of a cool tube produced tonal sound. According to Putnam and Dennis [1], studies in thermoacoustics began as early as 1777, when Byron Higgins [2] placed a hydrogen flame in a large pipe open at both ends, producing sound. Higgins noted that the acoustic oscillations produce by the tube depended upon the position of the flame. Later, in 1859, Rijke [3], as indicated by Feldman [4] and Bisio and Rubatto [5], investigated acoustic oscillations in a similar apparatus but with the hydrogen flame replaced by a mesh of heated metal wire (see Figure 1). He found that sound was only produced while the tube was in a vertical orientation and the heating element was in the lower half of the tube, indicating that the convective flow created by heating air in the pipe was important to its sound production. Furthermore, Rijke concluded that the sound produced was loudest when the mesh heater was a quarter of the tube length from the bottom. These investigations eventually led to pulse combustion technology, which is only somewhat related to the thermoacoustic device designed in this thesis.

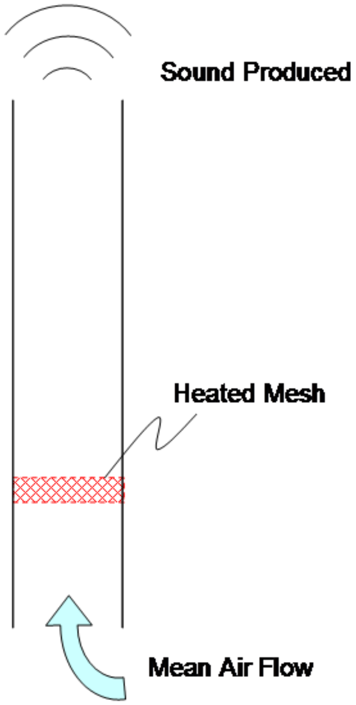

Figure 1. Rijke tube.

A more closely related area of thermoacoustics branched off a few years earlier, in 1850. According to Bisio and Rubatto [5], Sondhauss [6] experimented with a closed-open tube, as pictured in Figure 2, heating it by applying a flame to the bulb at the closed end to produce sound. Sondhauss explored the connection between the geometry of the resonating tube and the frequency of the sound produced. He noticed that the oscillation frequency was linked to the length of the tube and the volume of the closed end bulb. Furthermore, Sondhauss found that the sound was more intense when a hotter flame was applied. However, Sondhauss did not offer an explanation of the observations. A review of Sondhauss' work has been written by Feldman [7].

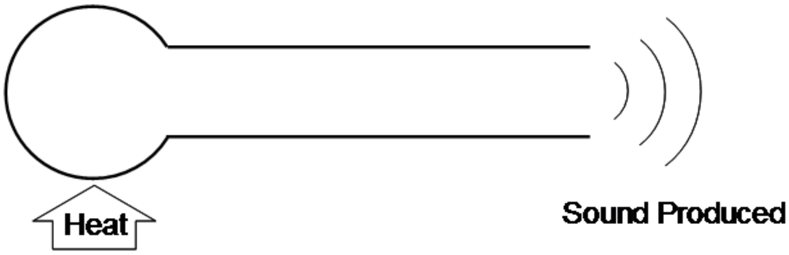

Figure 2. Sondhauss tube.

In 1949, another form of Sondhauss vibration was observed by Taconis et al. [8]. In working with liquid helium, a large temperature gradient was imposed on a glass tube. The temperature gradient, spanning from room temperature to cryogenic temperatures (~2°K), caused spontaneous oscillations inside the glass tube. These oscillations were later studied by Yazaki et al. [9]. Although Taconis provided an explanation of the oscillations, his qualitative theory was basically the same as that which had already been proposed by Lord Rayleigh many years earlier to account for observations of the Sondhauss tube. In 1896, Lord Rayleigh explained:

"For the sake of simplicity, a simple tube, hot at the closed end and getting gradually cooler towards the open end, may be considered. At a quarter of a period *before* the phase of greatest condensation …the air is moving inwards, ...and therefore is passing from colder to hotter parts of the tube; but the heat received at this moment (of normal density) has no effect either in encouraging or discouraging the vibration. The same would be true of the entire operation of the heat, if the adjustment of temperature were instantaneous, so that there was never any sensible difference between the temperatures of the air and of the neighboring parts of the tube. But in fact the adjustment of temperature takes *time*, and thus temperature of the air deviates from that of the neighboring parts of the tube, inclining towards the temperature of that part of the tube *from* which the air has just come. From this it follows that at the phase of greatest condensation heat is received by the air, and at the phase of greatest rarefaction heat is given up from it, and thus there is a tendency to maintain the vibrations." [10]

Rayleigh's criterion proved to be correct but did not include quantitative reasoning; however, he did refer to the work of Kirchoff, who studied the propagation of sound including thermal considerations.

The quantitative theory of thermoacoustics began with Kirchhoff [11] in 1868. He derived equations that accounted for thermal attenuation of sound as well as the normal viscous effects. Kirchhoff then applied his results to the case of a tube with a large radius so that the viscous and thermal effects due to the solid boundary could only be seen in a thin film of the fluid close to the wall. Slightly extending this work, Rayleigh [10] went on to consider narrow channels, but the theory was still only in the context of sound absorption.

Partly relying on Kirchhoff's work, Kramers [12] attempted to further develop thermoacoustic theory. In 1949, motivated by Taconis, Kramers derived a linear theory of thermoacoustics in an attempt to explain the behavior of sound in a tube with a temperature gradient; however, the resulting calculations were not in good agreement with experimental results, differing by orders of magnitude. Some of Kramers' early simplifying assumptions were found to be invalid.

In 1969, a major breakthrough came with Rott's investigation of thermoacoustics. Like, Kramers, Rott was primarily concerned with explaining Taconis oscillations, but Rott's efforts proved more fruitful. Publishing many papers on the subject [13–17], Rott developed a successful general linear theory of thermoacoustics. With this theory, thermoacoustic devices including both refrigerators and engines could be designed and investigated.

Although there are many categories of devices that apply thermoacoustic theory, thermoacoustic refrigerators (TARs) and thermoacoustic engines (TAEs), which are closely related, are particularly relevant to the present work. Investigation of TARs and TAEs began at Los Alamos National Laboratory (LANL) in the early 1980s. Wheatley, Swift, and Hofler among others are largely responsible for the new wave of advancements in practical thermoacoustic engines and refrigerators [18-21]. The first fully functioning thermoacoustic refrigerator was reported in Hofler's doctoral dissertation [22], where a standing-wave thermoacoustic refrigerator was built and investigated. Much of the development in theory is summarized by Swift [20].

Since the early work at LANL, many thermoacoustic devices have been constructed—some prototypes and a few for real applications; the following are a few notable examples. Tijani [23] designed and built a standing-wave TAR much like Hofler's but devoted more attention to the effects of varying certain parameters, such as working gas properties and stack size. Garrett et al. [24] developed a thermoacoustic refrigerator for cooling samples collected on space missions. Swift [25] designed a large thermoacoustic engine to drive an orifice pulse tube refrigerator, another kind of thermoacoustic device, which liquefied natural gas. Ballister and McKelvey [26] created a thermoacoustic device for cooling shipboard electronics. Backhaus and Swift [27] as well as others have experimented with traveling-wave thermoacoustic refrigerators, but such devices are not discussed in any detail here. As a last example, Adeff and Hofler [28] designed a TAR that was driven by a solar-powered thermoacoustic engine, creating a device containing no moving parts and whose operation was perfectly benign to the environment; most TARs use electrodynamic drivers, and electricity is mostly produced via fossil fuels. This thesis is concerned with standing-wave TARs, such as those investigated by Hofler and Tijani.

Current research in thermoacoustics focuses on the need to improve efficiency and power density. Therefore, one objective of this thesis is to compare the effects of different control schemes on TAR operation. While a few institutions are making progress, it is necessary for a wider research base to become involved before TARs and TAEs can be made commonplace. This thesis is one of the first in the field of thermoacoustics at the University of Pittsburgh, so the second objective is to create a sound basic knowledge of thermoacoustic refrigeration to aid future researchers at this institution.

1.2 A STANDING-WAVE THERMOACOUSTIC REFRIGERATOR

The configuration of standing-wave thermoacoustic refrigerators is simple. A standing-wave TAR comprises a driver, a resonator, and a "stack." To make the device practical, it must also utilize two heat exchangers; however, they are not necessary for creating a temperature difference across the stack. The parts are assembled as shown in Figure 3.

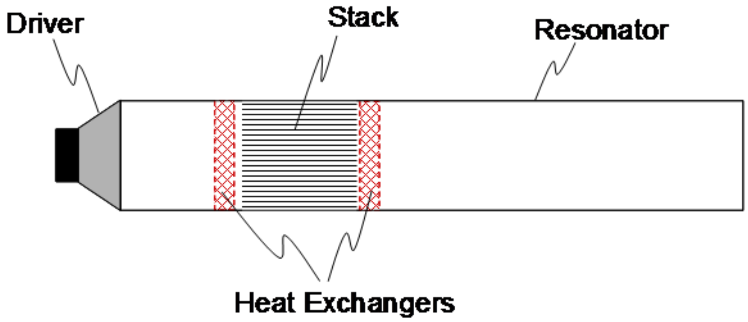

Figure 3. Configuration of a standing-wave thermoacoustic refrigerator.

The driver, which is often a modified electrodynamic loudspeaker, is sealed to a resonator. Assuming the driver is supplied with the proper frequency input, the resonator will respond with a standing pressure wave, amplifying the input from the driver. The standing wave drives a thermoacoustic process (see Sections 1.4 and 1.5) within the stack. The stack is so called because it was first conceived as a stack of parallel plates; however, the term “stack” now refers to the thermoacoustic core of a standing-wave TAR no matter the core’s geometry. The stack is placed within the resonator such that it is between a pressure antinode and a velocity antinode in the sound wave. Via the thermoacoustic process, heat is pumped toward the pressure antinode. The overall device is then a refrigerator or heat pump depending on the attachment of heat exchangers for practical application.

A temperature gradient can be created along the stack with or without heat exchangers. The exchangers merely allow a useful flow of heat. If the hot end is thermally anchored to the environment and the cold end connected to a heat load, the device is then a refrigerator. If the cold side is anchored to the environment and the load applied at the hot end, the device operates as a heat pump (heater). In any case, a few simple parts make up the thermoacoustic device, and no sliding seals are necessary.

1.3 MOTIVATION FOR THERMOACOUSTIC REFRIGERATION

The development of thermoacoustic refrigeration is driven by the possibility that it may replace current refrigeration technology. Thermoacoustic refrigerators, which can be made with no moving parts, are mechanically simpler than traditional vapor compression refrigerators and do not require the use of harmful chemicals.

Because of their simplicity, TARs should be much cheaper to produce and own than conventional technology. The parts are not inherently expensive, so even initial manufacturing costs should be low. Furthermore, mechanical simplicity leads to reliability as well as cheaper and less frequent maintenance. Until efficiency can be improved, operation costs may be higher; but with fewer moving parts, TARs require little to no maintenance and can be expected to have a lifetime much longer than ordinary refrigeration technology. Also, efficiency is likely to improve as thermoacoustic technology matures. Therefore, thermoacoustic refrigeration is likely to be more cost effective.

Besides reduced financial cost, environmental cost should be considered. Traditional vapor compression systems achieve their efficiencies through the use of specialized fluids that when released into the atmosphere (accidentally or otherwise) cause ozone depletion or otherwise harm the environment. Even most of the alternative fluids being developed cause harm in one way or another. For example, propane and butane won't destroy the ozone, but are highly flammable and pose a threat if a leak should occur. On the other hand, TARs easily accommodate the use of inert fluids, such as helium (see Section 2.1), that cause no harm to the environment or people in the event of a leak. Also, normal operating pressures for TARs are about the same as for vapor compression systems, so thermoacoustic refrigeration is just as safe in that respect. Furthermore, TARs can be driven by TAEs in which case the input power can come from any source of heat, including waste heat from other processes. Then the combination TAE/TAR device has no negative impact on the environment and, in fact, can utilize energy sources that are otherwise wasted. Overall, thermoacoustic refrigeration is much more benign than conventional refrigeration methods in terms of environmental and personal safety.

One drawback, however, is a lack of efficiency in current TARs when compared to vapor compression. Traditional refrigeration techniques have had the benefit of generations of research and application whereas thermoacoustic refrigeration is a new technology, so it is no wonder that vapor compression refrigerators are currently more efficient; however, there is reason to believe that thermoacoustic refrigeration will overtake vapor compression in the long run. The major reason is that a TAR can be driven with proportional control, but vapor compression schemes are binary (on/off). Although standing-wave TARs are currently less efficient than comparable conventional refrigerators, some of the difference can be made up when less than full power is required, which is most often the case. A normal refrigerator must switch off and on to maintain a given temperature; so the compressor is working its hardest whenever it is on, and the temperature actually oscillates around the desired value. In contrast, a refrigerator capable of proportional control, such as a TAR, can tune its power output to match the requirements of the load; so if the load increases a small amount, the refrigerator can slightly increase its power for a short time rather than running full tilt. This is especially advantageous in applications where thermal shocks can cause damage, such as cooling electronics. As indicated above, it is absolutely possible—if not probable—that with expanded research efforts, thermoacoustic technology will become more efficient than vapor compression.

Due to its advantages in mechanical simplicity and environmental and personal safety, thermoacoustic refrigeration is becoming more important in the research community and may soon reach a point in its development when it can replace vapor compression as the primary technology used in refrigeration applications.

1.4 BASIC THERMOACOUSTICS

Before introducing quantitative thermoacoustic theory, a simplified qualitative Lagrangian explanation of the thermoacoustic refrigeration cycle is helpful. Consider a parcel of gas in a channel between two plates, as in Figure 4, where the gas is acted upon by an acoustic standing wave. To keep things simple, the acoustic wave is considered a square wave and no losses are taken into account. There is a relatively small temperature gradient imposed on the walls of the channel such that the top is hot and the bottom cold. The thermoacoustic process can be conceptually simplified into four steps. First, the gas parcel undergoes adiabatic compression and travels up the channel due to the acoustic wave. The pressure increases by twice the acoustic pressure amplitude, so the temperature of the parcel increases accordingly. At the same time, the parcel travels a distance that is twice the acoustic displacement amplitude. Then the second step takes place. When the parcel reaches maximum displacement, it is has a higher temperature than the adjacent walls, assuming the imposed temperature gradient is sufficiently small. Therefore, the parcel undergoes an isobaric process by which it rejects heat to the wall, resulting in a decrease in the size and temperature of the gas parcel. In the third step, the second half-cycle of the acoustic oscillation moves the parcel back down the temperature gradient. The parcel adiabatically expands as the pressure becomes a minimum, reducing the temperature of the gas. The gas reaches its maximum excursion in the opposite direction with a larger volume and its lowest temperature. Finally, in step four, the parcel’s temperature has become lower than the local wall temperature (again assuming a small temperature gradient) so that heat flows from the wall to the gas parcel. The process then repeats so that small amounts of heat can be transported up the temperature gradient along the wall.

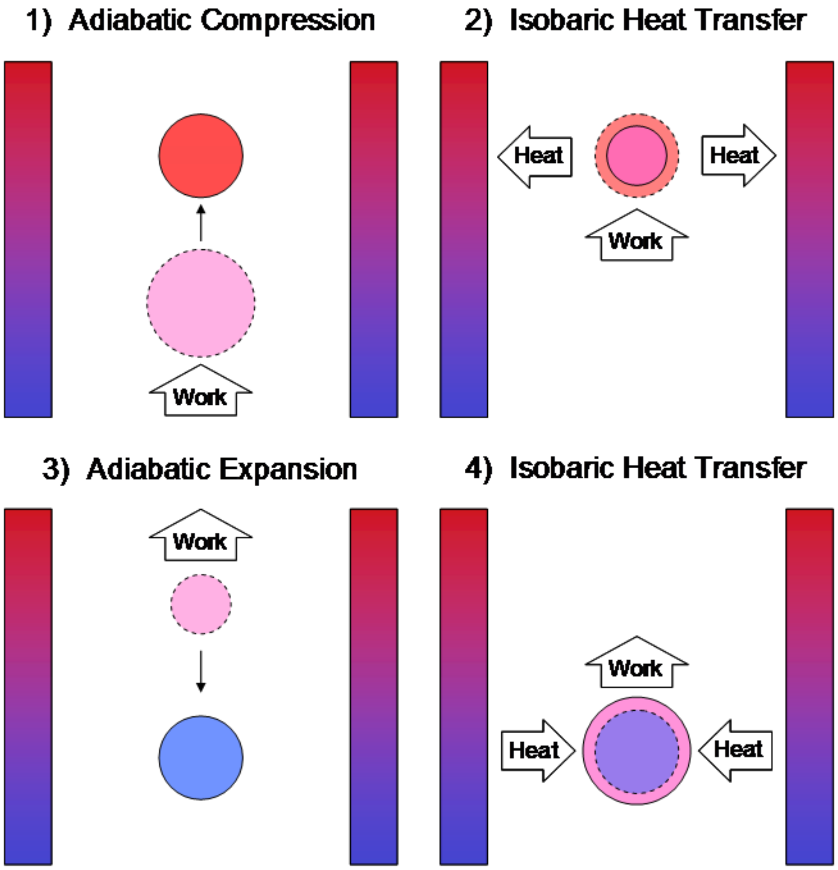

Figure 4. Simplified thermodynamic cycle experienced by a gas parcel in a thermoacoustic refrigerator.

Although the actual thermoacoustic process is much more complicated than this idealized description, this view of thermoacoustics yields a few useful ideas. Each gas parcel can only move a small amount of heat over a small temperature difference in this manner, so to move the heat across a larger temperature difference or move more heat (increase the power output), the situation must be modified. To move heat over a larger temperature difference, the length of the channel can be extended to allow more gas parcels to participate in moving the heat. Then, the temperature gradient is the same, but the total temperature difference increases. If the goal is to move more heat, then adding more channels in parallel will effectively increase the heat capacity of the gas so that the cooling/heating power of the process is increased. Alternatively, the working gas parameters can be modified so that its temperature fluctuates over a wider range, or the acoustic pressure can be increased to achieve the same effect.

Obviously, this cycle is useful for implementing a refrigerator or heat pump; but it is interesting to note that the same setup can yield an engine cycle. If the temperature gradient is sufficiently large, then the local wall temperature in the second step of Figure 4 will be higher than that of the adiabatically compressed gas. Therefore, the heat and work flows would be reversed. Likewise, in the fourth step, the gas parcel would reject heat to wall at the point of greatest rarefaction in the gas. This situation meets Rayleigh's (thermoacoustic) criterion such that the acoustic oscillation is encouraged. As a result, the only difference between a TAR and a TAE is the size of the temperature gradient across the stack.

If the temperature gradient perfectly matches the adiabatic temperature change in the gas, then there is no heat transfer in the second and fourth steps; the necessary temperature distribution is called the critical temperature gradient. If the gradient is smaller than this value, then the cycle will perform a heat pumping action; however, if the gradient is larger than the critical value, then the cycle will produce work in the form of an acoustic oscillation. Therefore, both TAEs and TARs utilize the same process, differing only in the temperature boundary condition. When losses are considered, the critical temperature gradient becomes a critical range rather than a single value so that no useful work is done in this range; acoustic power is absorbed and heat is moved down the temperature gradient.

As stated above, this Lagrangian view of thermoacoustics is extremely simplified. A more general linear theory of thermoacoustics is described in the next section.

1.5 GENERAL THERMOACOUSTIC THEORY

Linear acoustic theory, first developed by Rott [13-17], is applicable to both thermoacoustic refrigerators and engines; the only difference is the size of the temperature gradient along the stack. Before deriving the general theory, a few assumptions should be noted. Consider a single stack pore of arbitrary cross-section. The pore is taken to be long and narrow (of infinite length). A coordinate system is applied such that y and z are transverse coordinates and the x-axis lies in the longitudinal direction. The pore walls are considered rigid and their temperature a function of x alone. Furthermore, it is assumed that the walls have a sufficiently high heat capacity that their temperature is not locally affected by the temperature fluctuations in the gas. Note that all temperature-dependent physical parameters are implicitly dependent on x due to the temperature gradient in that direction. Finally, all acoustic variables are taken to be harmonic in time with radian frequency, ω. Following Arnott *et al.* [29], expressions for pressure, particle velocity, and heat and work flows will be derived. The fluid's acoustic variables (pressure, particle velocity, temperature, entropy, and density) can be expressed as

$$p(x,t) = p_0 + p_1(x)e^{-j\omega t} , \tag{1}$$

$$\mathbf{v}(x,y,z,t) = \left[\mathbf{v}_\tau(x,y,z) + v_x(x,y,z)\right]e^{-j\omega t} , \tag{2}$$

$$T(x,y,z,t) = T_0(x) + T_1(x,y,z)e^{-j\omega t} , \tag{3}$$

$$s(x,y,z,t) = s_0(x) + s_1(x,y,z)e^{-j\omega t} , \tag{4}$$

and

$$\rho(x,y,z,t) = \rho_0(x) + \rho_1(x,y,z)e^{-j\omega t} , \tag{5}$$

respectively. The subscript *0* indicates a mean value, and the subscript *1* indicates a first-order (acoustic) value. In Equation (2), $\mathbf{v}_\tau$ is the transverse particle velocity, and v_x is the longitudinal particle velocity.

There are three governing equations in thermoacoustics; they are the momentum (Navier-Stokes) equation, the continuity equation, and the energy equation. In order, these equations are expressed as

$$\rho\left[\frac{\partial \mathbf{v}}{\partial t}+(\mathbf{v}\cdot\nabla)\mathbf{v}\right]=-\nabla p+\mu\nabla^2\mathbf{v}+\left(\xi+\mu/3\right)\nabla(\nabla\cdot\mathbf{v}), \tag{6}$$

$$\frac{\partial p}{\partial t}+\nabla\cdot(\rho\mathbf{v})=0, \tag{7}$$

and

$$\frac{\partial}{\partial t}\left(1/2\,\rho\mathbf{v}^2+\rho\varepsilon\right)=-\nabla\cdot\left[\rho\mathbf{v}\left(1/2\,\mathbf{v}^2+h\right)-K\nabla T-\mathbf{v}\cdot\mathbf{\Sigma}\right], \tag{8}$$

where μ and ξ are shear and bulk viscosity, respectively; ε and h are internal energy and enthalpy per unit mass, respectively; K is the gas's thermal conductivity; and $\boldsymbol{\Sigma}$ is the viscous stress tensor with components given by

$$\Sigma_{ij}=\mu\left(\frac{\partial v_i}{\partial x_j}+\frac{\partial v_j}{\partial x_i}\right)+\left(\xi-\frac{2}{3}\mu\right)\delta_{ij}\,\frac{\partial v_k}{\partial x_k}. \tag{9}$$

Because the pore is long and narrow, the variation of acoustic parameters is much greater in the transverse directions than along the *x*-axis so that partial derivatives with respect to *x* are negligible compared to derivatives in transverse directions. With this approximation in mind, Equations (6-8) can be expanded using Equations (1-5) and reduced to first-order, resulting in the following approximate equations for the *x* components of momentum, continuity, and heat transfer, respectively [29]:

$$-j\omega\rho_0 v_x = -\frac{dp_1}{dx} + \mu\nabla_\tau^2 v_x , \tag{10}$$

$$-j\omega\rho_1 + \frac{\partial}{\partial x}\left(\rho_0 v_x\right) + \rho_0 \nabla_\tau \cdot \mathbf{v}_\tau = 0 , \tag{11}$$

and

$$-j\omega\rho_0 c_p T_1 + \rho_0 c_p v_x \frac{\partial T_0}{\partial x} = -j\omega\beta T_0 p_1 + K\nabla_\tau^2 T_1 , \tag{12}$$

where the transverse Laplacian and gradient operators are defined as $\nabla_\tau^2 = \frac{\partial^2}{\partial y^2} + \frac{\partial^2}{\partial z^2}$ and $\nabla_\tau = \frac{\partial}{\partial y}\hat{\mathbf{y}} + \frac{\partial}{\partial z}\hat{\mathbf{z}}$, c_p is the isobaric heat capacity per unit mass, and $\beta = -\frac{1}{\rho_0}\left(\frac{\partial \rho}{\partial T}\right)_p$ is the thermal expansion coefficient.

Before proceeding, it is convenient to define the shear wave number as $\lambda_v = 2r_h\sqrt{\frac{\rho_0\omega}{\mu}}$ and the thermal disturbance number as $\lambda_k = 2r_h\sqrt{\frac{\rho_0\omega c_p}{K}}$, where r_h is the hydraulic radius (cross-sectional area divided by perimeter) of the pore. Assuming v_x is of the form

$$v_x = \frac{1}{j\omega\rho_0}\frac{dp_1}{dx}F\left(y, z, \lambda_v\right), \tag{13}$$

where $F\left(y, z, \lambda_v\right)$ is dependent upon pore geometry and is left to be determined later, Equation (10) implies that $F\left(y, z, \lambda_v\right)$ must satisfy

$$F\left(y, z, \lambda_v\right) - j\left(\frac{2r_h}{\lambda_v}\right)^2 \nabla_\tau^2 F\left(y, z, \lambda_v\right) = 1 \tag{14}$$

and the boundary condition $F = 0$ at the pore wall. This result is set aside for the time being, and Equation (12) is manipulated, using Equation (13) and the thermodynamic relation

$T_0\beta^2 / c_p = (\gamma - 1)/a^2$, where γ is the ratio of specific heats (isochoric to isobaric), and a is the adiabatic sound speed in the fluid, to obtain

$$T_1 - j\left(\frac{2r_h}{\lambda_k}\right)^2 \nabla_\tau^2 T_1 = \frac{\gamma - 1}{a^2\rho_0\beta} p_1 - \frac{F(y, z, \lambda_\nu)}{\rho_0\omega^2}\frac{dT_0}{dx}\frac{dp_1}{dx}. \tag{15}$$

Now, assuming T_1 can be written such that

$$T_1 = G_a(y, z, \lambda_k)\frac{\gamma - 1}{a^2\rho_0\beta} p_1 - G_b(y, z, \lambda_k, \lambda_\nu)\frac{1}{\rho_0\omega^2}\frac{dT_0}{dx}\frac{dp_1}{dx}, \tag{16}$$

Equation (15) can be separated into two equations as follows

$$G_a - j\left(\frac{2r_h}{\lambda_k}\right)^2 \nabla_\tau^2 G_a = 1 \tag{17}$$

and

$$G_b - j\left(\frac{2r_h}{\lambda_k}\right)^2 \nabla_\tau^2 G_b = F(y, z, \lambda_\nu). \tag{18}$$

Applying the boundary condition T_1 = 0 on the pore boundary, yields $G_a = 0 = G_b$ on the pore boundary; and by inspection of Equation (14), the solution to Equation (17) is

$$G_a(y, z, \lambda_k) = F(y, z, \lambda_k). \tag{19}$$

Using this result and Equations (17) and (14), it can be shown that the solution to Equation (18) is given by

$$G_b(y, z, \lambda_k, \lambda_\nu) = \frac{F(y, z, \lambda_k) - \sigma F(y, z, \lambda_\nu)}{1 - \sigma}, \tag{20}$$

where σ is the Prandtl number of the fluid. The acoustic temperature variation is then

$$T_1 = \frac{(\gamma - 1)}{a^2\rho_0\beta}\mathrm{F}(\mathrm{y,z,}\lambda_\mathrm{k})p_1 - \frac{1}{\rho_0\omega^2}\frac{F(y, z, \lambda_k) - \sigma F(y, z, \lambda_\nu)}{1 - \sigma}\frac{dT_0}{dx}\frac{dp_1}{dx}. \tag{21}$$

The first-order thermodynamic equation of state for density is

$$\rho_1(x,y,z) = \frac{c_p}{T_0}T_1 - \frac{\beta}{\rho_0}p_1, \tag{22}$$

which, in light of Equation (21), becomes

$$\begin{aligned}\rho_1(x,y,z) = {} & \frac{\gamma - (\gamma-1)F(y,z,\lambda_k)}{a^2}p_1 \\ & + \frac{\beta}{\omega^2}\frac{dT_0}{dx}\frac{F(y,z,\lambda_k) - \sigma F(y,z,\lambda_\nu)}{1-\sigma}\frac{dp_1}{dx}\end{aligned}. \tag{23}$$

To develop longitudinal heat and work flow equations, previous quantities must be averaged over the cross-sectional area of the pore. To this end, the area-averaged continuity equation becomes

$$-j\omega\rho_1(x) + \rho_0(x)\frac{dv_z(x)}{dx} - \beta\rho_0(x)v_x(x)\frac{dT_0}{dx} = 0. \tag{24}$$

where

$$v_x(x) = \frac{1}{j\omega\rho_0}\frac{dp_1}{dx}F(\lambda_\nu) \tag{25}$$

is the particle velocity averaged over the pore cross-section and *F(·)* is equivalent to the cross-sectionally averaged *F(y,z,·)*. Using an area-averaged form of Equation (23), the equation for area-averaged pressure can be obtained as

$$\rho_0\frac{d}{dx}\left(\frac{F(\lambda_\nu)}{\rho_0}\frac{dp_1}{dx}\right) + \frac{\beta\left[F(\lambda_k) - F(\lambda_\nu)\right]}{1-\sigma}\frac{dT_0}{dx}\frac{dp_1}{dx} + \frac{\omega^2}{a^2}\left[\gamma - (\gamma - 1)F(\lambda_k)\right]p_1 = 0. \tag{26}$$

This expression applies to a single pore, which is acceptable for pressure and particle velocity as these quantities are not summed over all of the pores in a stack; however, longitudinal heat and work flows do depend on the total open area in the stack, A_o. The total time-averaged longitudinal energy flow to second order is

$$\dot{H}(x) = \dot{Q}(x) + \dot{W}(x) - \dot{Q}_{loss}(x) \tag{27}$$

where $\dot{Q}$ is time-averaged heat flow from hydrodynamic transport, $\dot{W}$ is time-averaged acoustic power, and $\dot{Q}_{loss}$ is time-averaged heat flow lost to conduction down the temperature gradient in the stack. These quantities are given by

$$\dot{Q} = \frac{A_o}{2}\,\mathrm{Re}\left[\frac{1}{A}\int_A \rho_0 c_p v_x(x,y,z)T_1^*(x,y,z) - \beta T_0 v_x(x,y,z)p_1^*(x)dydz\right], \tag{28}$$

$$\dot{W} = \frac{A_o}{2}\,\mathrm{Re}\left[\frac{1}{A}\int_A v_x(x,y,z)p_1^*(x)dydz\right], \tag{29}$$

and

$$\dot{Q}_{loss} = \left(A_o K + (A - A_o)K_s\right). \tag{30}$$

where A is the total cross-sectional area of the stack and K_s is the thermal conductivity of the solid stack material. Introduction of Equations (13) and (21) yields

$$\dot{Q} = \frac{A_o}{2}\frac{\rho_0 c_p}{A}\,\mathrm{Im}\left[\int_A \frac{\gamma - 1}{\omega a^2 \rho_0^2 \beta} G_1 \frac{dp_1}{dx} p_1^* + \frac{1}{\omega^3 \rho_0^2 (1-\sigma)} \frac{dT_0}{dx}\frac{dp_1}{dx}\left(\frac{dp_1}{dx}\right)^* (\sigma G_2 - G_1)dydz\right] - \beta T_0 \dot{W} \tag{31}$$

and

$$\dot{W} = \frac{A_o}{2A}\,\mathrm{Im}\left[\int_A \frac{F(y,z,\lambda_\nu)}{\omega\rho_0}\frac{dp_1}{dx} p_1^* dydz\right] \tag{32}$$

where $G_1 = F(y,z,\lambda_\nu)F^*(y,z,\lambda_k)$, $G_2 = F(y,z,\lambda_\nu)F^*(y,z,\lambda_\nu)$, and * indicates complex conjugation. Carrying out the integrations yields

$$\dot{Q} = \frac{A_o}{2}\frac{\beta T_0}{\omega\rho_0}\left(\mathrm{Im}\left[\frac{F^*(\lambda_k) - F(\lambda_\nu)}{1+\sigma}\frac{dp_1}{dx}p_1^*\right] - \frac{c_p}{\beta T_0 \omega^2}\left|\frac{dp_1}{dx}\right|^2 \frac{dT_0}{dx}\mathrm{Im}\left[\frac{F^*(\lambda_k) + \sigma F(\lambda_\nu)}{1-\sigma^2}\right]\right)$$

(33)

and

$$\dot{W} = \frac{A_o}{2}\mathrm{Im}\left[\frac{F(\lambda_\nu)}{\omega\rho_0}\frac{dp_1}{dx}p_1^*\right]. \tag{34}$$

These are general equations for heat and work flow in the stack, and can be used for design. In Section 2.4.4, dimensionless forms of these equations are used to determine the length and position of the stack in the resonator.

The function *F* is dependent on pore geometry. Arnott *et al.* [29] present several examples of *F* for different geometries. Most investigations in thermoacoustic refrigeration utilize parallel plate geometries, in which case the area-averaged *F(·)* is given by

$$F(\lambda) = 1 - \frac{2}{\sqrt{-i}\,\lambda}\tanh\left(\frac{\sqrt{-i}\,\lambda}{2}\right). \tag{35}$$

This function can be compared to Swift's notation [20] by noting that $F^*(\lambda) = 1 - f$, where f is Rott's function. This relationship applies to both thermal and viscous functions and for all pore geometries. As discussed in Section 2.4, this work utilizes a square pore geometry, which has [29]

$$F(\lambda) = \frac{64}{\pi^4}\sum_{m,n\,odd}\frac{1}{m^2 n^2 Y_{mn}(\lambda)}. \tag{36}$$

where

$$Y_{mn}(\lambda) = 1 + \frac{i\pi^2}{\lambda^2}\left(\frac{m^2+n^2}{4}\right). \tag{37}$$

2.0 DESIGN OF A STANDING-WAVE TAR

In designing a standing-wave TAR, there are many parameters to consider, including the stack length and position, pore size and geometry, driver parameters, resonator dimensions, working gas properties, and operating conditions. To begin design, a few choices must be made to reduce the number of variables. Often the first step is selecting a working gas because it is much easier to design other parameters around the physical properties of a fluid than to find or create a fluid with the physical properties dictated by choosing other parameters first. Next, the average operating pressure should be chosen as it is fairly independent of other parameters and can be easily adjusted as needed. Even after these preliminary choices, the other parameters are not fully constrained. A starting point must be chosen to add further constraints to the rest of the TAR parameters. The stack is an appropriate place to begin, as it is often made of a material that is both expensive and difficult to machine; and it may be difficult to construct a stack to meet predetermined specifications. Once a few of the stack parameters are chosen, the resonator can be designed accordingly. From there, a driver can be chosen. There are, of course, some situations in which a different design strategy may be better, but this method was appropriate here as certain resources, i.e. helium and a porous ceramic material, were already on hand. For this work, some of the components and parameters were chosen for convenience and cost reduction as will be noted in their corresponding sections.

2.1 WORKING GAS

The working gas should be chosen to have a large thermal penetration depth, δ_k, and a small viscous penetration depth, δ_v. Thermal penetration depth is a measure of how well a fluid can transfer heat through its boundary. A large thermal penetration depth allows for more heat transfer between the stack walls and the gas, increasing the overall efficiency of the TAR. A fluid's viscous penetration depth can be viewed as a measure of the frictional losses within the fluid. A small viscous penetration depth indicates that losses per unit area due to viscous effects will be lower, which is important in the many small pores of the stack where the surface area is large. The thermal and viscous penetration depths are related by a fluid's Prandtl number, defined as

$$\sigma = \frac{\delta_v^2}{\delta_k^2}. \tag{38}$$

A lower Prandtl number is desirable as it indicates that gains with respect to thermal considerations will outweigh the viscous losses [30].

It is also desirable that the working gas have a large ratio of isobaric to isochoric specific heats, γ. When this ratio is large, a larger temperature gradient across the stack can be achieved because the maximum temperature difference is approximately proportional to (γ-1) [22]. The ratio of specific heats of an ideal gas can be expressed in terms of the degrees of freedom of one of its molecules as

$$\gamma = \frac{f+2}{f}, \tag{39}$$

where *f* is the number of degrees of freedom. Equation (39) shows that monatomic gases are best suited for creating large temperature gradients because such gases have only three degrees of freedom, the fewest possible.

In many cases, helium is chosen for its low Prandtl number ($\sigma = 0.68$), and its large ratio of specific heats ($\gamma = 5/3$, as it is monatomic). Furthermore, helium has very good thermal conductance and is cheaper and easier to work with than are other noble gases. Sometimes helium is used as part of a mixture containing other gases, such as argon, to enhance the desired properties. However, because this project was a first attempt, helium alone was chosen for simplicity; its properties at the chosen pressure are given in Table 1. Although some of these properties are temperature/pressure dependent, the changes in temperature and pressure are considered to be much smaller than the average values, so the working gas's properties can be taken as constant.

Table 1. Properties of helium.

Thermal conductivity, K	0.138 W/(m*K)
Ratio of specific heats, γ	5/3
Isobaric specific heat, c_p	5193.2 J/(kg*K)
Prandtl number, σ	0.68
Specific ideal gas constant, R_s	2077

2.2 MEAN PRESSURE

Mean pressure, p_0, is proportional to the power density of a thermoacoustic refrigerator [31]. For this reason, it is desirable to choose a large average pressure; however, other factors limit the pressure, including the mechanical strength of the resonator and the effect of pressure on the thermal penetration depth.

Higher pressures require a stronger pressure vessel. Designing a stronger resonator often leads to more expensive materials and a heavier, bulkier overall TAR. In addition to these drawbacks, a higher internal pressure makes it more difficult to seal the working gas inside. Sealing the TAR can be especially problematic when working with helium due to its small molecular size. Other TARs with relatively large internal pressures have required the use of exotic materials, such as indium o-rings [22, 23] to deal with helium leakage.

Another consideration is the effect of pressure on the thermal penetration depth. The thermal penetration depth is inversely proportional to the square root of the mean pressure, so as pressure increases, the thermal penetration depth shrinks. For a given stack pore size, this trend results in decreasing efficiency. If the pore size is designed around the mean pressure, this problem can be countered by using smaller pores; however, using smaller pores makes the stack increasingly difficult to manufacture. Furthermore, smaller pores lead to more viscous dissipation of energy as there is more solid surface area in contact with the working fluid. Therefore, the choice of mean pressure must balance its effects on power density, resonator design, and stack design.

As cost was of some importance to the current endeavor, the mean pressure was chosen to be 1 atmosphere, or 101 kPa. Although the resonator could certainly have held higher pressures, other effects needed to be considered. Using atmospheric helium greatly reduced the risk of leakage thereby eliminating the need for expensive seal materials. Furthermore, because this TAR utilized a stack that was found rather than manufactured, using higher pressures would have required a lower operation frequency to counter the effect on the thermal penetration depth (see Section 2.4.3). A lower operating frequency would have decreased the efficiency of the driver and increased the required resonator length. Therefore, for a first attempt at designing a TAR, atmospheric pressure seemed to be the best choice.

2.3 DRIVE RATIO

The drive ratio, D, is defined as the acoustic pressure amplitude, p_1, divided by the mean pressure, p_m. This ratio should be kept sufficiently low so as to avoid acoustic nonlinearities such as turbulence. Specifically, the dimensionless Mach number, M, should be smaller than about 0.1 [20], and the Reynolds number, R_y, should be smaller than 500. Tijani [31] uses the following definition of the Mach number:

$$M = \frac{p_1}{\rho_m a^2}; \tag{40}$$

where a is the adiabatic speed of sound, and ρ_m is the density for the mean operating conditions; however, a more readily useable form was derived and is given by

$$M = \frac{D}{\gamma}. \tag{41}$$

This formulation seems to be better suited for use with the dimensionless equations in designing the stack (see Section 2.4.4). Given $\gamma = \frac{5}{3}$, the drive ratio must be less than 16.7% to ensure that $M < 0.1$ and less than 10.0% to ensure that $R_y < 500$. Because the chosen mean pressure is 101 kPa, the acoustic pressure amplitude must be less than 10 kPa, a large number for a normal loud speaker, the intended driver. The actual drive ratio for a loud speaker is more likely to be on the order of a few percent. Therefore, to proceed with calculations it was assumed that $D = 0.01$ so that the actuator would not need to be driven excessively hard to achieve the calculated cooling power and efficiency.

2.4 THE STACK

The stack must be able to efficiently convert the acoustic pressure oscillations into a temperature gradient. It is desirable for the stack material to have a low thermal conductivity and greater heat capacity than the working gas. Furthermore, the geometry of the pores must be designed by balancing the thermal efficiency and viscous losses within the stack via the thermal and viscous penetration depths. The stack length and its position in the resonator can be determined from equations for the heat and work flows.

2.4.1 Stack Material

A stack material should be selected first so that its properties can be taken into account while choosing other parameters. The material chosen should have a low thermal conductance. As a TAR's main purpose is to move heat from one end of the stack to the other, heat conduction in the opposite direction (from the hot end to the cold end) results in a reduction of efficiency. If the thermal conductivity is too high, the situation is analogous to carrying water uphill with a leaky bucket. The material should also have a larger specific heat capacity than the gas. A stack with a larger heat capacity is less affected by the temperature oscillations of the nearby gas, which is desirable because it allows the temperature gradient along the stack walls to remain steady, increasing the effectiveness of the gas in transporting thermal energy from the cold end to the hot end of the stack.

Due to the necessary thermal properties, ceramic and plastic materials are often chosen as stack materials. Normally, the machineability of the stack material is a major consideration as channels are generally very small and difficult to create without fracturing the material. Ceramic materials, especially, are generally brittle and extremely difficult to machine. Consequently, ceramics are not often used in thermoacoustic applications unless they can be produced in the appropriate configuration. Often plastic materials are chosen because they are a bit easier to work with. For example, a plastic strip can be wound around a rod, keeping space between the layers with fishing line [22, 23]. The result is a spiral stack, which approximates a parallel plate stack. Even with plastic materials, however, the necessarily small tolerances of pore geometry can make manufacturing a stack an unattractive option.

For this stack, a ceramic material was chosen because it was readily available in a form that would require little modification to create an appropriate stack. Intended for use in a vehicle's catalytic converter, the ceramic came as a cylinder with square channels running parallel to its axis. While placing some restrictions on other parameters, as noted in Section 2.4.3, the low cost in terms of the time and money required for machining, or otherwise manufacturing, a stack was extremely attractive.

2.4.2 Pore Geometry

The shape of the channels, or pores, can affect the efficiency of the stack in converting acoustic work into cooling power. By considering an inviscid approximation, it has been shown that heat and work flows are proportional to the negative of the imaginary part of Rott's function f_k [18, 29]. Therefore, it is desirable to obtain a large negative imaginary portion of this function. Figure 5 shows Re(f_k) and Im(f_k) for various geometries versus the ratio of the pore's hydraulic radius, $r_{h,}$ to the thermal penetration depth, δ_k. The hydraulic radius is defined as the area of a pore divided by its perimeter. In the case of parallel plates, the hydraulic radius is taken as one half of the space between plates. The code used to generate this plot can be found in Appendix A.1.

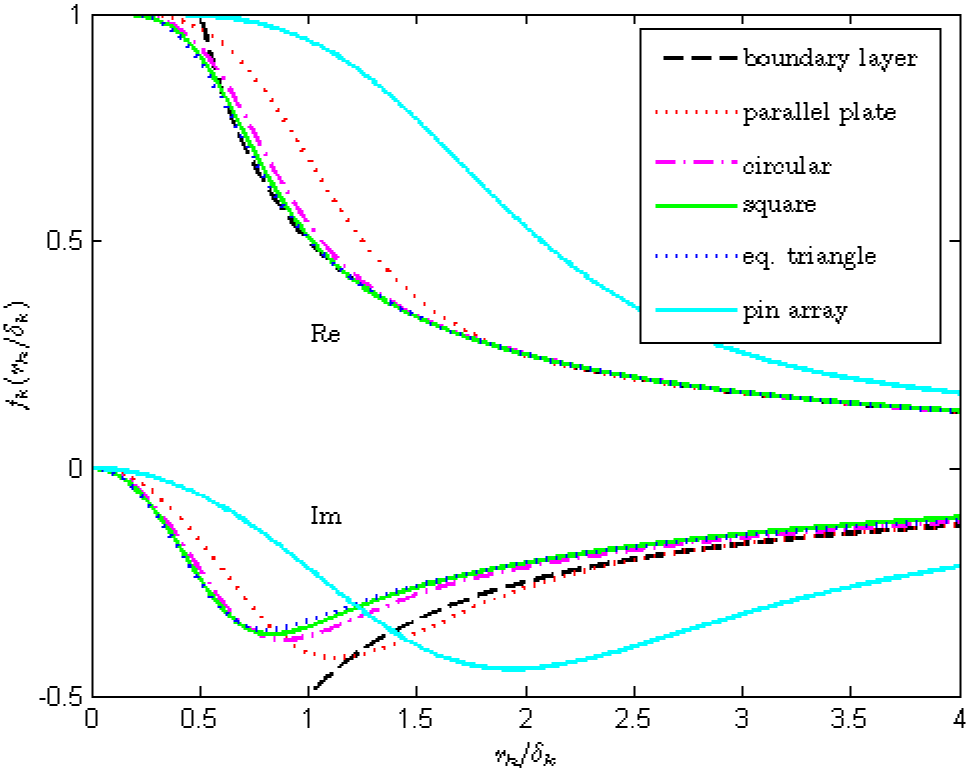

Figure 5. Imaginary and real parts of f_k.

In Figure 5, the boundary layer approximation is shown. For all pore geometries, Rott's function approaches $f_k = (i-1)\delta_k/2r_h$ for "large" $r_h/\ \delta_k$. The plot gives an idea of when this approximation is appropriate for the various geometries shown.

According to the negative of the imaginary part of Rott's function, the best stack geometry is actually a pin array [32, 33]; however, such stacks are more difficult to manufacture than stacks with other geometries. Therefore, a pin array stack was not considered a viable option for this project.

Next to a pin array, the best geometry is a stack of parallel plates. Manufacturing this kind of stack is much more manageable. For example, parallel plates can be achieved using chemical etching techniques [22], or parallel plates can be approximated by a spiral wound stack [22, 23, 34]. Furthermore, all other things being equal, parallel plate stacks can allow approximately 10% more heat and work flows than stacks with closed cross-section pores [29].

In the end, parallel plate geometry was not used because a square pore stack could be made much more readily and cheaply. A monolithic piece of ceramic with parallel square channels was given to the project. The only necessary adjustment was to decrease the overall diameter and length of the monolith to suit the design of the resonator and optimize efficiency.

2.4.3 Pore Size

The size of the pores is dependent upon the thermal penetration depth. The pores should be designed so that the working gas and stack walls can transfer heat as effectively as possible. To that end, the pores should be as small as possible so that more gas is within a thermal penetration depth of a stack wall, thus making good thermal contact between the stack walls and the gas. On the other hand, small pores create more surface area where losses occur and may cause turbulence, disrupting the acoustic field. These factors may affect the efficiency of the device significantly and need to be balanced.

Following from Figure 5, the negative of the imaginary part of f_{k} for a square pore is maximized when the ratio of hydraulic radius to thermal penetration depth is approximately $r_h/\ \delta_k = .83$, so this is the optimal ratio for facilitating the thermoacoustic process; however, a spacing between $2\delta_k$ and $4\delta_k$ is suggested in order not to disturb the acoustic field near the stack [19]. Also, because the hydraulic radius is actually fixed for this stack, owing to material selection, a lower ratio would imply a larger penetration depth; and, as shown below, a larger thermal penetration depth necessitates a larger resonator for the given choices of working gas and mean pressure.

The thermal penetration depth of the working gas can be calculated as

$$\delta_k = \sqrt{\frac{2K}{\rho c_p \omega}}\,, \tag{42}$$

where K is the gas's thermal conductivity, ρ is its density, c_p is its isobaric specific heat, and ω is the operating frequency in radians per second. For a given mean pressure, K, ρ, and c_p can be considered constant as the acoustic pressure will be relatively small. Therefore, the thermal penetration depth is proportional to the inverse of the square root of the operating frequency. Because the resonator will be designed to create a standing wave, the effective length of the resonator must be inversely proportional to operating frequency. Thus, the resonator length, assuming a straight tube resonator, is directly proportional to the square of the thermal penetration depth. It follows that with a fixed hydraulic pore radius, the resonator length increases with smaller ratios of $r_h/\ \delta_k$. Then, for overall compactness of the TAR, the thermal penetration depth should be small; however, as previously stated, the thermal penetration depth should be large to allow more effective heat transfer between the working gas and stack walls. Considering these conflicting objectives, it was determined that a ratio of $r_h/\ \delta_k = 3$ would be appropriate. Because the spacing of the channels in the stack material was 1.1 mm, this ratio yielded a thermal penetration depth of .37 mm. Using Equation (42) and the properties of helium listed in Table 1, this penetration depth corresponds to an operating frequency of about 365 Hz. As indicated by Figure 5, a slight increase in the thermal penetration depth is more desirable than a slight decrease, corresponding to a slight decrease or increase of operating frequency, respectively. Therefore, during construction, it was deemed better to err on the side of creating a lower frequency resonator. Code was written in Matlab® to facilitate recalculation of the operating frequency for different parameters; this code can be found in Appendix A.2.

2.4.4 Stack Length and Position

With a known frequency of operation, dimensionless heat and work flow equations were used to calculate and plot performance curves for various stack lengths and positions relative to the speaker. These equations were derived from the exact partial differential equations by making some simplifying assumptions [20, 31]. The dimensionless forms of these equations, as derived by Tijani *et al.* [31], further simplify the design process. Although the dimensionless forms were not absolutely necessary, they are included here to allow future design endeavors to follow a different path.

The main assumptions made in the derivation from the exact equations are the short-stack and boundary-layer approximations [20]. The short-stack approximation states that the length of the stack is much less than the acoustic wavelength at the TAR's operating frequency. The boundary-layer approximation is used to greatly simplify the coupled equations governing the fluid motion and heat transfer. These assumptions have a few implications. First, the velocity and pressure of the gas can be considered constant over the length of the stack [20]. Although no thermoacoustic effect would take place if pressure was constant, this approximation is acceptable because, if the stack is sufficiently short, the variation in pressure from one end to the other is small in comparison to the full acoustic pressure amplitude, p_1. Next, under the approximations, it is assumed that the temperature difference across the stack, ΔT_m, is much less than the average absolute temperature, T_m. This assumption allows the thermophysical properties of the working gas and stack to be taken as constants within the stack [20]. Away from the stack, temperature should only vary by the acoustic temperature amplitude, which is even smaller than the temperature difference across the stack. It follows that the thermophysical material properties can be considered constant everywhere, simplifying the general equations.

With these assumptions in mind, Swift [20] derived equations for heat and work flows in a thermoacoustic element. Borrowing from Olson and Swift [35], Tijani [36] later normalized the parameters involved as shown in Table 2, where A is the cross-sectional area of the resonator around the stack, y_0 is half a pore diameter, k is the acoustic wave number, and x is distance measured from the driver face. Using these dimensionless parameters, Tijani then derived the following dimensionless equations for the heat and work flows respectively:

$$\dot{Q}_{cn} = -\frac{\delta_{kn} D^2 \sin(2x_{sn})}{8\gamma(1+\sigma)\Lambda}\left(\frac{\Delta T_{mn}\tan(x_{sn})}{(\gamma-1)BL_{sn}}\frac{1+\sqrt{\sigma}+\sigma}{1+\sqrt{\sigma}} - \left(1+\sqrt{\sigma}-\delta_{kn}\sqrt{\sigma}\right)\right) \tag{43}$$

and

$$\dot{W}_n = \frac{\delta_{kn}L_{sn}D^2}{4\gamma}\left[(\gamma-1)B\cos^2(x_{sn})\left(\frac{\Delta T_{mn}\tan(x_{sn})}{BL_{sn}(\gamma-1)\left(1+\sqrt{\sigma}\right)\Lambda}-1\right)-\frac{\sqrt{\sigma}\sin^2(x_{sn})}{B\Lambda}\right], \tag{44}$$

where Λ is used as an intermediate variable and is defined as

$$\Lambda = 1-\delta_{kn}\sqrt{\sigma}+\frac{1}{2}\sigma\delta_{kn}^2 . \tag{45}$$

It should be noted that Equation (43) ignores axial thermal conduction in the stack [31]. Assuming that the stack material is chosen such that its thermal conductivity is low, the neglected term would be much smaller than the transverse heat transfer between the stack wall and the gas. Therefore, it is assumed that axial heat transport is due to the thermoacoustic effects alone.

Table 2. Normalized parameters used in dimensionless work and heat flow equations.

Operation parameters

Drive ratio: $D = p_1 / p_m$
Norm. cooling power: $\dot{Q}_{cn} = \dot{Q}_c / p_m aA$
Norm. acoustic power: $\dot{W}_n = \dot{W} / p_m aA$
Norm. temperature difference: $\Delta T_{mn} = \Delta T_m / T_m$

Gas parameters

Norm. thermal penetration depth: $\delta_{kn} = \delta_k / y_0$

Stack Geometry

Norm. stack length: $L_{sn} = kL_s$
Norm. stack center position: $x_{sn} = kx_s$
Porosity: $B = y_0^2 / (y_0 + l)^2$

To relate Tijani's dimensionless equations to a physical system and determine an appropriate stack length and center position, the pore geometry, operating frequency, working gas properties, mean pressure, and target temperature difference must be known. Then, once the proper dimensionless values are determined, they can be inserted into Equations (43-45), and the normalized cooling power and normalized required acoustic power can be calculated for various values of stack length, L_s, and stack center position, x_s, measured from the speaker face. Because the actual cooling power and acoustic power are normalized by the same factor, the actual coefficient of performance, COP can be calculated using the normalized values. The COP of a refrigeration system is given by

$$COP = \frac{\dot{Q}_c}{\dot{W}}, \tag{46}$$

where $\dot{W}$ is the required power input from the operator. The COP, often referred to as performance, does not take into account any input power supplied by the environment and, therefore, should not be confused with the thermodynamic efficiency of the device. When no input is supplied by the environment, the COP and efficiency are the same, but in general, the quantities are different. In the case of a thermoacoustic stack, the power input by the operator is the acoustic power supplied by the speaker, so the COP can be calculated as

$$COP = \frac{\dot{Q}_{cn}}{\dot{W}_n}. \tag{47}$$

This value is plotted in Figure 6 for the parameters chosen up to this point in the design process.

Due to the fragility of the ceramic, the stack length was chosen to be L_s = 0.064 m (2.5 in.). Before the entire design was completed, the stack material was cut to 3 inches for some preliminary testing. Once the stack length was reduced, it was much more difficult to cut the material again while avoiding breakage. As a result, a length of 0.064m was chosen to allow a reasonable reduction in stack length while ensuring the material could be cut fairly easily. Although a shorter stack could achieve a higher COP, as seen in Figure 6, cutting the ceramic to a smaller length probably would have resulted in fracture, rendering the material unusable. It should be understood that although the choice of stack length was constrained, one can choose either stack length or position somewhat arbitrarily unless there are other design specifications to be met, such as a certain cooling power or COP; so an optimal design was still possible.

Because the stack length was prematurely determined, only the stack position was left to determine the COP. Figure 6 shows that for a stack length of 0.064 m the maximum achievable COP is about 2.9 and corresponds to a stack center position of x_s = 0.112 m from the speaker face. Therefore, the hot end of the stack was placed $0.112m - \frac{1}{2}(0.064m) = 0.080m$ from the speaker, and the cold end of the stack was at $x = 0.144m$.

Equations (43-45) rely on an assumed temperature gradient (the target temperature difference chosen here was 30 °K), so it is of interest to know the actual cooling power and acoustic power required to achieve that temperature gradient. These power values, however, are dependent on the cross-sectional area of the stack as well as the acoustic drive ratio, p_1/p_m. If the TAR had been designed to achieve a specific cooling power, as is likely in practical applications, then the cross-sectional area of the stack would have been determined by choosing a COP and solving for the area via the normalized cooling power. Furthermore, the acoustic power required to achieve the specified COP, cooling power, and temperature gradient can be found in the same manner via the normalized acoustic power.

For the present study, the cross-sectional area of the stack was determined by the resonator diameter because actual cooling power was not of major concern. It was deemed more beneficial to make the resonator out of easily accessible materials and shape the ceramic stack to the resonator than to choose a cooling power to determine the cross-sectional stack area and then have to custom form a resonator. This approach was appropriate because the device was not required to meet stringent design specifications. With that in mind, the stack diameter was chosen to be 4 inches to match the intended resonator material, polyvinylchloride (PVC) pipe (see Section 2.5.1). Then the cross-sectional area of the stack was calculated as

$A = \frac{1}{4}\pi(4in.)^2 \approx 12.57 sq.in. = 0.008107 m^2$. This value was used to rescale the normalized cooling power and acoustic power and plot the actual values, shown in Figures 7 and 8, respectively. In Figure 7, it is seen that a cooling power of just over 1.4 W is expected for the given parameters, and according to Figure 8, an input acoustic power of just under 0.5 W should be required to achieve the chosen temperature gradient and calculated cooling power.

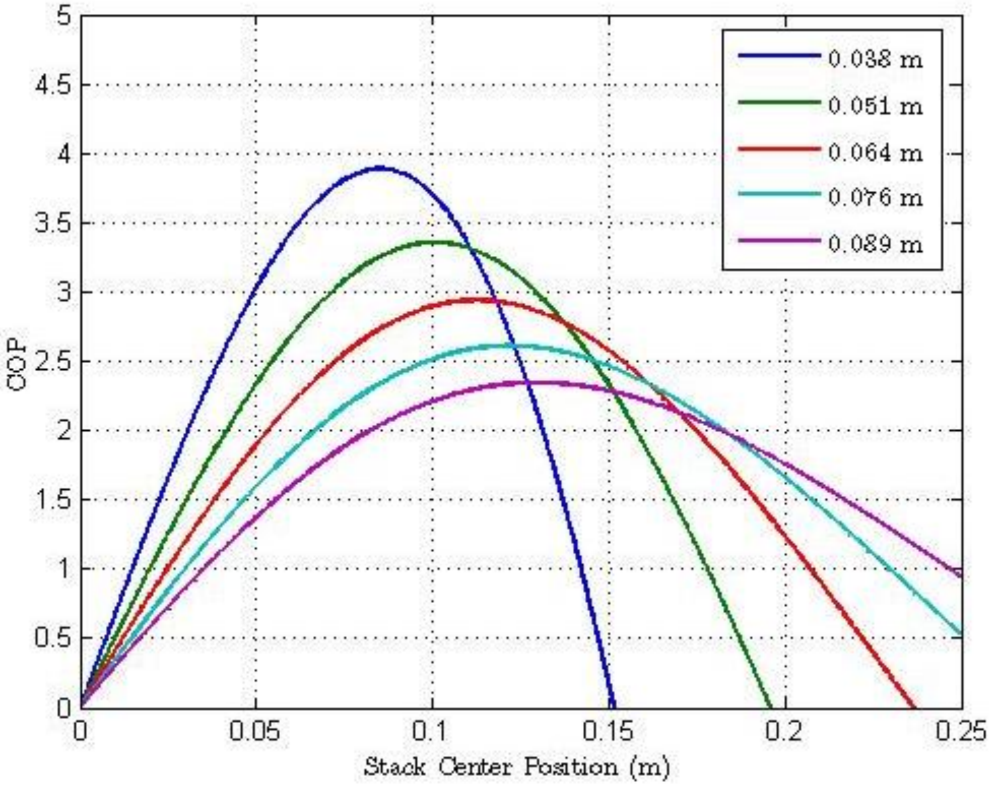

Figure 6. Coefficient of performance vs. stack center position for various stack lengths.

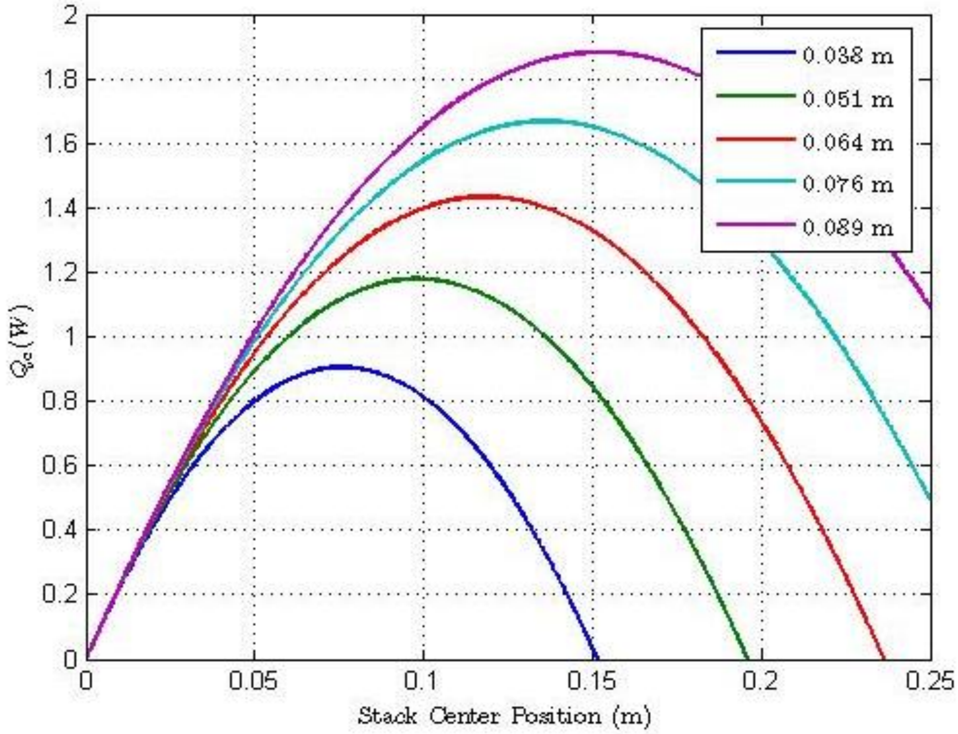

Figure 7. Cooling power vs. stack center position for various stack lengths.

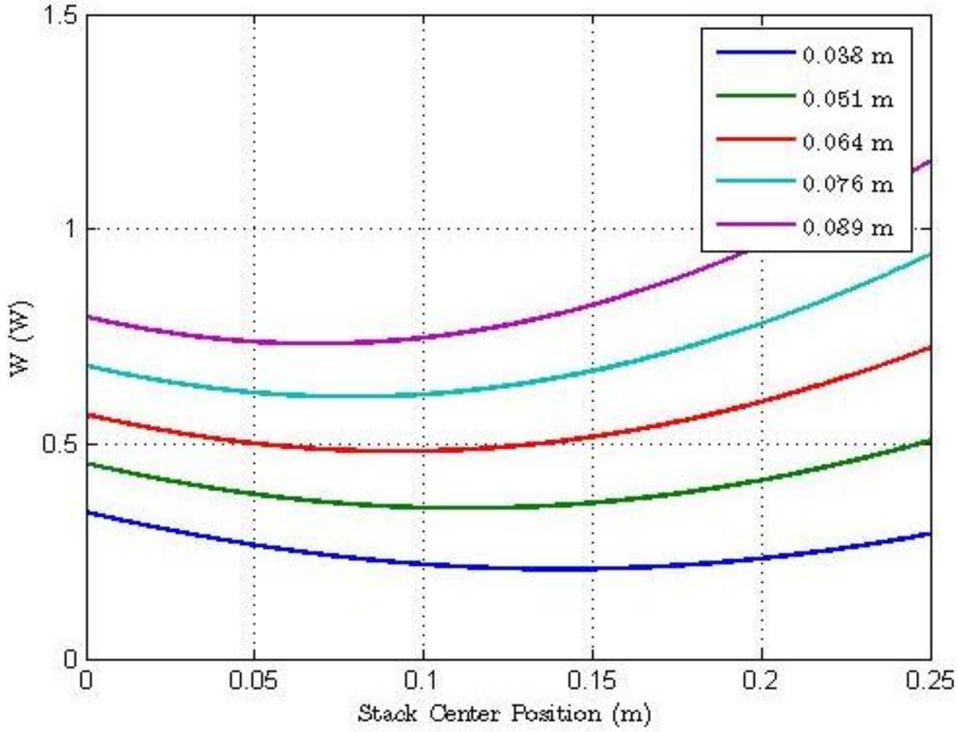

Figure 8. Acoustic power vs. stack position for various stack lengths.

At this point in the design process, it should be kept in mind that the equations used to derive the cooling power and acoustic power are based on several simplifying assumptions and an arbitrary temperature gradient. The actual performance of any TAR will be less than ideal, and the TAR should not be expected to fully achieve the efficiency or cooling power given by the calculations. Cooling power can be increased by applying more acoustic power, but it is more difficult to compensate for lacking efficiency; therefore, it is suggested that the more general heat and work equations [20] be numerically integrated to create a more accurate design for future endeavors. Programs, the most notable of which is DeltaEC [37], are available to aid in numerical integration for a wide variety of thermoacoustic applications.

2.5 THE RESONATOR

Having chosen an operating pressure, frequency, and stack parameters, the resonator can be designed. The resonator should be made of an acoustically reflective material that is sufficiently strong for the desired operating pressure. The possibilities of working fluid and thermal leakage should also be considered. Regardless of the resonator material the thermal and viscous losses at the interior wall of the resonator must be minimized by the design to ensure maximal efficiency of the thermoacoustic refrigerator.

2.5.1 Resonator Materials

There are three areas to consider when choosing a resonator material: mechanics, acoustics, and heat transfer. Mechanical strength is fairly straightforward. The resonator material simply must be strong enough and impermeable enough (especially when dealing with helium) to contain the gas at the maximum pressure. For some materials, these constraints may lead to thicker resonator walls, increasing the bulk and weight of the TAR, but there are a wide variety of materials that are mechanically suited to be pressure vessels. Acoustically, the resonator material should have large impedance so that the working gas sees it as a rigid boundary, and losses in the acoustic pressure wave are minimal. The characteristic impedance of a material is proportional to its density, so dense materials, such as metals, make good acoustic resonators. Metals also tend to make very good pressure vessels because of their high strength to weight ratios.

However, a metal resonator in a thermoacoustic application would have disadvantages. Metals' high thermal conductivities would allow heat transfer from the environment to the cold side of the resonator. A heat leak in the cold side of the resonator would require that some of the stack's available cooling power be used to move that heat across the stack and back into the environment at the hot end, which is a waste of energy that shows up in the heat flow equation as an extra thermal load [38]. For this reason, a material with low thermal conductivity should be chosen for the resonator. However, it is desirable for the gas in the cold end of the resonator to be in good thermal contact with the cold end of the stack because it allows the system to reach steady state more quickly. The system can respond faster because heat can flow to the stack via the thermal conduction of the wall, which can be much faster than conduction through the gas, thus keeping the temperature uniform away from the stack. Therefore, a material with high thermal conductivity is desirable on the interior of the resonator away from the stack. Around the stack, the resonator should have very low thermal conductivity, even on the interior, to prevent heat leaking from the hot side of the resonator back to the cold side. For overall thermal considerations, a resonator should have a low thermal conductivity; although thermal conductance is desirable in certain places, when a single material is to be used, that concern is far outweighed by the need to prevent unwanted heat transfer, known as parasitic heat loss.

The reasoning described above, combined with the objectives of low cost and simple construction, led to the choice of using PVC pipe to make the resonator. PVC pipe is readily available and has a low thermal conductivity (0.19 W/m-°K). Also, pressure-rated PVC piping is readily available and comes in a variety of sizes. For this project, the pressure rating turned out to be relatively unimportant because the mean pressure was atmospheric, but in the early stages of design, higher pressures were considered. Even 6 inch diameter pipe, rated for a maximum operating pressure of over 180 psi, is strong enough to withstand the pressures used in most thermoacoustic applications (many TARs operate with about 150 psi of internal pressure). The drawbacks of using PVC are that it is not as acoustically resonant as other materials, for example, steel, and it is fairly permeable to helium. As there was no objective for cooling power, the acoustic losses were not a primary concern; and because the operating pressure was atmospheric, the helium would slowly diffuse but not readily leak out of the vessel. The final factor in choosing PVC was the ease with which PVC pipe and fittings can be machined and assembled. Specifically, 4-inch pipe was chosen for the stack and driver part of the resonator as that is also a common speaker size. Other sizes were then used as described in Section 2.5.2.

2.5.2 Resonator Geometry

The resonator geometry is partly determined by the length and position of the stack and partly determined by the operating frequency. While designing the stack and its position in the standing wave, it was determined that the cold end of the stack would be 0.1435 m from the speaker face; 4-inch diameter pipe was chosen for the stack section of the resonator, but the remaining resonator geometry still required a bit of design work.

A standing wave resonator can be a half- or a quarter-wavelength, referring to the first acoustic mode, as shown in Figure 9(a) and (b), respectively. The first acoustic mode is most often utilized because a higher mode implies an unnecessarily long resonator, leading to more losses associated with the resonator surface area as discussed below. In Figure 9, the red lines indicate the spatial velocity profiles, and the blue lines represent the spatial pressure profiles for the first acoustic mode. Although the velocity of the gas at the speaker face will be nonzero, it is smaller than the velocity of the gas elsewhere and can be neglected. A half-wavelength resonator is simply a tube closed at both ends so that the velocity vanishes at the endpoints. A quarter-wavelength resonator is half as long but still resonates at the same frequency because the end away from the driver is open; the pressure there is zero, but the velocity is a maximum. Therefore, the same pressure and velocity profile can be obtained with a shorter pipe, which will have less surface area on which losses occur. Some researchers have even tried to create a resonator that is shorter than one quarter-wavelength by using a secondary driver to match the impedance of the missing portion [39].

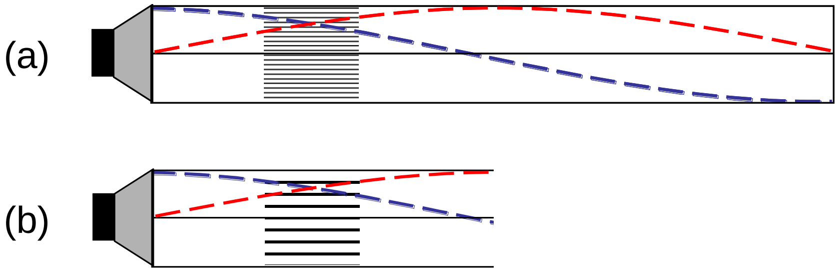

Figure 9. Resonator types: (a) half-wavelength resonator; (b) quarter-wavelength resonator.

In general, shorter/smaller resonators are better for thermoacoustic applications because there are fewer losses. Resonator losses are due to viscous dissipation and thermal relaxation along the wall in the boundary layer, defined by the viscous and thermal penetration depths. As a consequence of the boundary layer approximation, the power loss per unit surface area can be written as [20, 22, 31]

$$\frac{d\dot{W}_{loss}}{dS} = \frac{1}{4}\rho_m |u_1|^2 \delta_\nu \omega + \frac{1}{4}\frac{|p_1|^2}{\rho_m a^2}(\gamma - 1)\delta_\kappa \omega \,, \tag{48}$$

where u_1 is the particle velocity. The first and second terms of Equation (48) represent viscous losses and thermal losses, respectively. The viscous losses are a consequence of shear forces in the working gas dissipating kinetic energy; the thermal losses are due to thermal relaxation in the boundary layer. As can be seen from Equation (48), the total of these two loss mechanisms is proportional to the surface area of the resonator. Therefore, a reduction in the surface area of a resonator leads to an increase in efficiency.

There are two ways to minimize the surface area of a standing wave TAR that have been widely used [22, 24, 31]; the first is to make use of the quarter-wavelength resonator geometry, and the second is to reduce the resonator diameter at the cold end of the stack, as shown in Figure 10; this geometry is sometimes called a “Hofler resonator.” Obviously, the open end of an ideal quarter-wavelength resonator cannot contain pressures above 1 atm, so the boundary condition at that end must be simulated with an enclosed buffer volume. As a result, the resonator will be somewhere between a quarter- and half-wavelength. If a large enough volume is used, the resonator will be a bit longer than a quarter-wavelength but still much shorter than a half-wavelength, so the overall surface area of the resonator is greatly reduced. To further diminish the resonator surface area, the section of the resonator between the cold end of the stack and the buffer volume can be decreased in diameter. As it turns out, to retain the desired operating frequency, the length of this resonator section must also be reduced, further decreasing the total surface area.

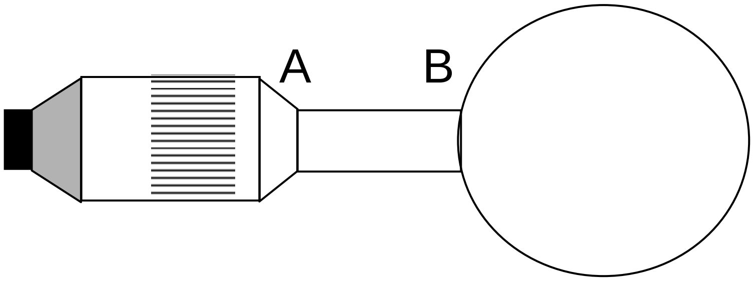

Figure 10. Resonator optimized for minimized losses per unit surface area.

Impedance matching can be used to determine the optimal length and diameter of the cold section of the resonator [22, 31]. First, the buffer volume is assumed large enough to be considered an open termination of the small diameter tube, and the transition between the large and small diameter tubes is assumed to be an abrupt transition. Then, the acoustic velocity and pressure amplitudes, respectively *u* and *p*, in the tubes can be expressed as

$$p^{(1)} = p_1^{(1)} \cos(kx), \tag{49}$$

$$u^{(1)} = \frac{p_1^{(1)}}{\rho_m a} \sin(kx), \tag{50}$$

$$p^{(2)} = p_1^{(2)} \cos(kx'), \tag{51}$$

$$u^{(2)} = \frac{p_1^{(2)}}{\rho_m a} \sin(kx'), \tag{52}$$

where the superscript *(1)* refers to the large diameter tube near the driver, *(2)* refers to the small diameter tube, and L_T is the total length of both tubes. The variable x' is shifted from x so that similar equations can be used to describe the pressures and velocities. Equations (51) and (52) are then used in the integration of Equation (48) to find the total losses in the small diameter tube, $\dot{W}_{loss}^{(2)}$. Normalizing $\dot{W}_{loss}^{(2)}$ by

$$N = \frac{\pi d^{(1)} \delta_v a \left(p_1^{(1)}\right)^2}{8\gamma p_m} \tag{53}$$

yields [22]

$$\frac{\dot{W}_{loss}^{(2)}}{N} = \frac{d^{(2)}}{d^{(1)}} \left(\frac{p_1^{(2)}}{p_1^{(1)}} \right)^2 \left[\left(1 + \frac{\gamma - 1}{\sqrt{\sigma}} \right) k\left(x'_B - x'_A\right) + \frac{1}{2}\left(1 - \frac{\gamma - 1}{\sqrt{\sigma}} \right) \left(\sin\left(2kx'_A\right) - \sin\left(2kx'_B\right) \right) \right], \tag{54}$$

where d is the pipe diameter, the subscript A refers to the transition between the large and small diameter pipes, and the subscript B refers to the transition between the small diameter pipe and the buffer volume as noted in Figure 10. The normalization constant, N, is derived from the losses in the large diameter tube, neglecting the presence of the stack and any heat exchangers. Because the buffer volume is assumed to be large, $kx'_B \approx \frac{\pi}{2}$ so there is a pressure node and velocity antinode at transition B.

Now, the acoustic impedance, Z, of each section can be found according to [40]

$$Z = \frac{p}{Su}, \tag{55}$$

where S is the cross-sectional area of the given tube; so

$$Z^{(1)} = \frac{ia\rho_m}{S^{(1)}} \cot(kx) \tag{56}$$

and

$$Z^{(2)} = \frac{ia\rho_m}{S^{(2)}} \cot(kx'). \tag{57}$$

For the desired resonance, the impedances must match at transition A. After evaluating the impedances at transition A and imposing equality, the shifted coordinate, x'_A, can be solved for in terms of x_A, giving

$$kx'_A = \tan^{-1}\left(\left(\frac{d^{(1)}}{d^{(2)}}\right)^2 \tan(kx_A)\right). \tag{58}$$

Then, imposing pressure continuity at transition A,

$$\frac{p_1^{(2)}}{p_1^{(1)}} = \frac{\cos(kx_A)}{\cos(kx'_A)}. \tag{59}$$

Using Equations (58) and (59) and the large buffer volume approximation, Equation (54) can be plotted for varying pipe diameter ratios as shown in Figure 11. The green dashed line represents viscous losses, the red dotted line represents thermal losses, and the solid blue line is the sum of the two loss mechanisms. The length of the large diameter pipe, x'_A, is chosen to be 0.190 m, which is slightly longer than the distance from the speaker to the cold end of the stack. The extra length ensures that there is adequate space for instrumentation. Given constant parameters for the large diameter section, the optimum small diameter is about 0.57 times the large diameter. A small diameter of 2 inches was chosen because that pipe size and its associated couplings are more common than 2.5-inch pipe and couplings; both sizes introduce only a small amount of loss due to the suboptimal diameters. Equation (54) predicts an increase in losses of less than 2% in the small diameter pipe with the use of 2-inch pipe.

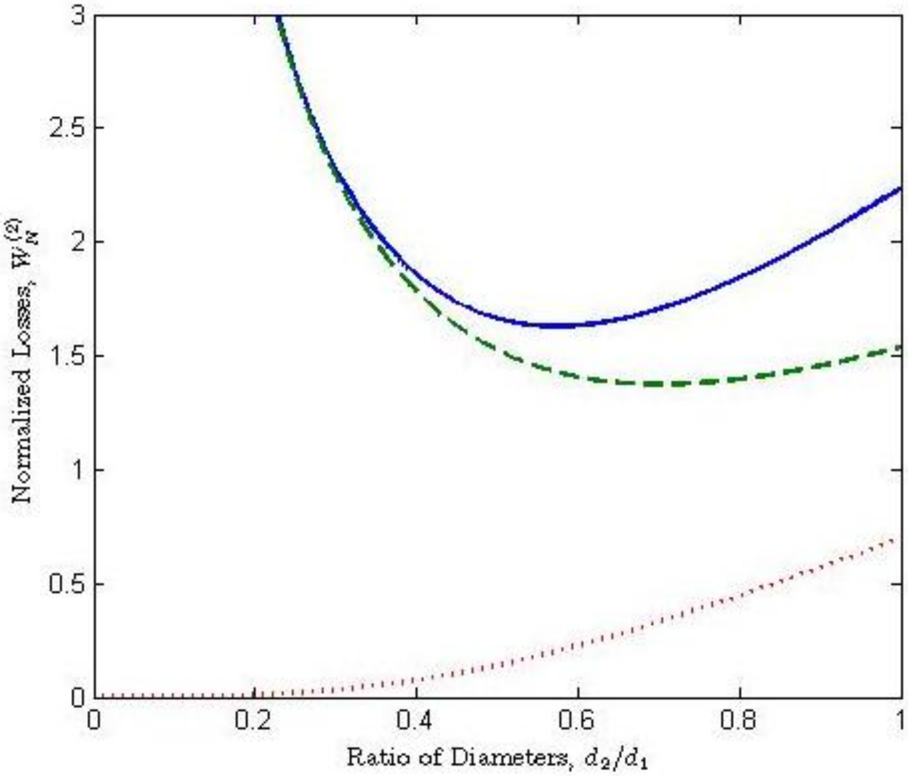

Figure 11. Plot of normalized losses in small diameter section of resonator as a function of the ratio of the small and large diameters.

With the small diameter chosen, the length of the small section can be calculated using Equation (58) and the assumption that $kx'_B \approx \frac{\pi}{2}$. For a diameter ratio of 0.5, the length of the small diameter pipe should be $x'_B - x'_A = 0.2107$ meters. Then, the overall length of the resonator is 0.4007 m plus the length of the buffer volume.

The buffer volume size can be determined by matching its impedance to the end of the small diameter tube [22], but the decision to use off-the-shelf PVC pipes and fittings prevented much accuracy in the buffer volume's design. Because PVC fittings are available only in certain standard sizes, it was difficult to make an accurate buffer volume without modifying parts and, therefore, compromising the structural integrity of the resonator. It was assumed that a buffer volume at least as large as the volume of the rest of the resonator would sufficiently approximate the open end condition required for a quarter-wavelength resonator. As indicated in the literature [22, 31, 41], it is beneficial to gently taper the transition from the small diameter pipe to the full diameter of the buffer volume as the taper prevents separation of the boundary layer from the wall, known as jetting, when gas moves into the buffer volume. A taper with an included angle of about 20° is acceptable as this angle yields a sufficient pressure recovery coefficient and a fairly low loss coefficient [41]. With the above remarks as a rough guide, the design of the buffer volume was determined by available materials in the construction phase. The taper had a divergence half-angle of about 11° and was 0.235 m long. The remaining part of the buffer volume was made to approximate a sphere with a diameter of about 6 inches. A more detailed description of the buffer volume can be found in Section 3.1.

2.6 THE DRIVER

The driver of a thermoacoustic refrigerator must be able to supply sufficient acoustic pressure to develop an appreciable temperature difference across the stack. Most drivers have been custom made or modified electroacoustic transducers [22, 24, 31, 42], but any form of acoustic power production can be used. For simplicity, an off-the-shelf loudspeaker is sometimes used [39]. For this project, the driver was an unmodified loudspeaker. Although the chosen driver was not optimized for this application, the following discussion is included for future reference.

Ideally, the sum of the mechanical reactance of the speaker and the mechanical reactance of the resonator is zero in order to maximize either overall power or efficiency [43]. This can be done by setting both individual reactances to zero, or by making them equal in magnitude but opposite in sign. In either case, the speaker suspension stiffness can be adjusted to achieve the desired mechanical reactance in the driver. Stiffening the suspension can involve replacing the cone and/or the surround of the speaker with a different material so that the mechanical reactance disappears at the desired frequency. The electrical reactance of the driver is still nonzero but can be eliminated by adding a series capacitor [43]; then, the input impedance seen by the driving amplifier is purely real. Removing the reactance of the overall system allows for optimum electroacoustic power production or efficiency.

To fully optimize the driver, the effective area of the speaker cone must be designed for maximum electroacoustic efficiency or maximum power. Wakeland [43] found that the electroacoustic efficiency, η, of a TAR driver can be calculated by

$$\frac{1}{\eta}=\frac{R_e R_m}{(Bl)^2}\frac{R_m}{R_a}\left(1+\frac{R_a}{R_m}\right)^2+\left(1+\frac{R_m}{R_a}\right)+\frac{R_e R_m}{(Bl)^2}\frac{X^2}{R_m R_a}, \tag{60}$$

and the time-averaged acoustic power, Π_a, at maximum sustainable driver current, I_{max}, is

$$\Pi_a(I_{\max})=\frac{(Bl\cdot I_{\max})^2}{2}\frac{R_a}{(R_m+R_a)^2+X^2}, \tag{61}$$

where R_e is the electrical resistance of the driver, R_m is the mechanical resistance of the driver, R_a is the mechanical resistance of the acoustic resonator, X is the sum of the driver's and resonator's mechanical reactances, and Bl is the force factor of the driver. After setting the derivatives of Equations (60) and (61) with respect to R_a to zero, it is seen that

$$(R_a)_{\eta_{\max}}=R_m\sqrt{\frac{(Bl)^2}{R_e R_m}+1} \tag{62}$$

gives the optimum value of R_a for electroacoustic efficiency, and

$$(R_a)_{\Pi_{\max}} = R_m \tag{63}$$

is the optimum value for acoustic power production. R_a is related to the effective driver area, S, by the expression

$$R_a = S^2 \operatorname{Re}[Z], \tag{64}$$

where Z is the complex acoustic impedance of the resonator. The size of the speaker face can then be chosen to maximize either acoustic power or electroacoustic efficiency. It is important to note that this value of S for maximum achievable power is based on the maximum sustainable current; however, in practice, the driver displacement is likely to be the limiting factor in acoustic power output [43].

An alternative to modifying the driver area is optimizing the operating frequency to suit a fixed driver area. The analysis above assumes a fixed acoustic resistance, but because Z is generally a function of frequency, it may be possible to choose an operating frequency such that R_a meets the requirement of Equation (62) or (63) [43]. Due to the decision to use an unmodified loudspeaker for simplicity, the effective driver area was predetermined. The electroacoustic efficiency could have been maximized by selecting an appropriate operating frequency, but this choice would have been in conflict with the operating frequency chosen to maximize the effectiveness of the thermoacoustic stack. It was decided that the effectiveness of the stack was more important than the electroacoustic efficiency of the driver. Because only modest acoustic power would be required, the lower driver efficiency could be compensated by supplying more electrical power without burning out the voice coil. For future work, either the driver or stack should be modified so that both can operate at the same optimum frequency.

3.0 CONSTRUCTION OF THE THERMOACOUSTIC REFRIGERATOR

The thermoacoustic refrigerator designed in the previous section was constructed from readily available materials. The resonator and a speaker box were made by chemically welding various PVC pipes and fittings. The stack material was cut to length and chipped down to the proper diameter then secured in the resonator. Although it was not rigorously designed, a heat exchanger was made and inserted into the resonator at the hot end of the stack. The driver was used as found except that its flange was slightly modified to fit the bolt holes of the resonator. Finally, the refrigerator was instrumented. The completed TAR is shown in Figure 12.

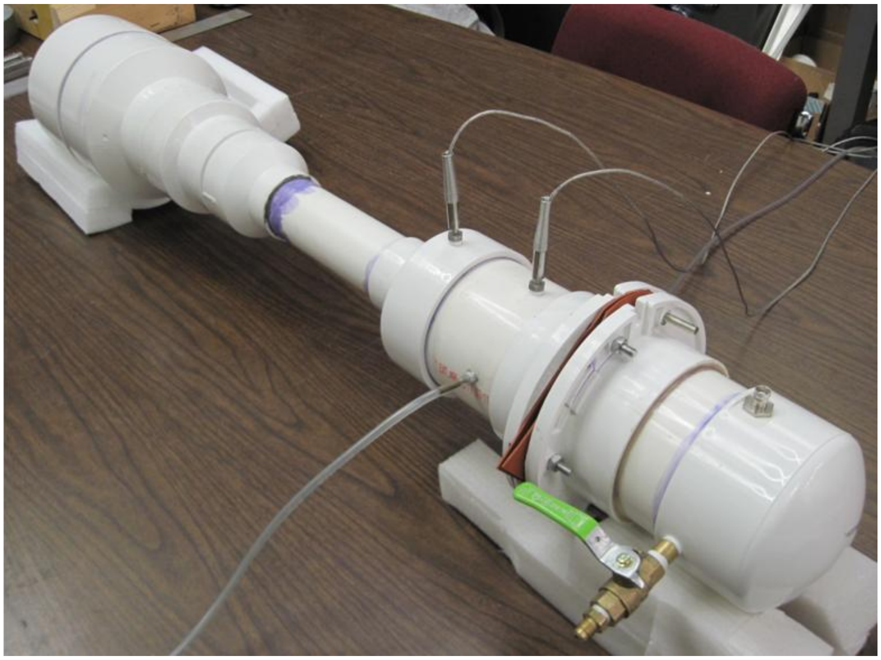

Figure 12. Fully assembled thermoacoustic refrigerator.

3.1 THE RESONATOR

The portion of the resonator nearest the speaker was chosen to be 4 inches in diameter. This choice allowed the speaker to closely fit the driver end of the resonator; also, standard PVC flanges could be used where the resonator and driver housing would meet. A 4-inch schedule 40 PVC pipe was cut to 17cm in length so the stack could be placed the appropriate 8.0 cm from the driver end of the resonator while leaving enough room for a thermocouple to later be inserted into the resonator at either end of the stack. A flange was solvent welded to the driver end of the 4-inch pipe using Oatey® Purple Primer (#30756) and Marsh Laboratories PVC Cement (#PH-100/Clear).

Next, the stack was cut to length on a band saw and shaped by hand. The length was 6.4 cm (see Section 2.4.4) and the cross-section had to be reduced to a 4-inch diameter circle. The ceramic material could be cut transversely with a band saw, but much more care was needed to cut it in a direction parallel to the material's axis. A miniature hacksaw was used to remove the bulk of the excess material, but the ceramic tended to fracture if not cut along the grid formed by the cross-section of the square channel array. To refine the stack into a cylinder, a very small screwdriver was used to chip away at the ceramic, one channel at a time. Although somewhat tedious, this method of making a stack was fairly easy.

After the heat exchanger was in place (see Section 3.2), the stack was inserted into the 4-inch pipe and secured at the designated distance from the driver end of the resonator, which was accomplished using a small amount of epoxy resin; the cold end of the stack was just over 2.5 cm from the opposite end of the cut pipe. The end of the 4-inch pipe opposite the driver was welded into a 4-inch by 2-inch reducer. The rest of the resonator, including the small diameter section and the buffer volume, was assembled separately and later solvent welded to the 4-inch by 2-inch reducer.

The buffer volume and taper were constructed from reducer fittings and an end cap that were joined using the shortest possible lengths of the corresponding pipe sizes. The taper started as a 2-inch by 3-inch coupling joined via a 3-inch sch. 40 pipe to a 3-inch by 4-inch coupling. To smooth the transition, PC Plumbing® epoxy putty was molded onto the interior surface of the 3-inch pipe to create a conical section. The putty was allowed to cure and was ground smooth. Then, a short section of 4-inch pipe was cemented into the large end of the 4-inch coupling, and a 4-inch by 6-inch coupling was cemented to the other end of the 4-inch pipe. More epoxy putty was used to continue the taper and make a complete conical section increasing from 2 inches to 6 inches in diameter. The buffer volume was then completed by adding a short section of 6-inch pipe and capping the end.

The small diameter section of the resonator was 2-inch sch. 40 PVC pipe and was cut to 21.1 cm as dictated by the design. One end of this pipe was then solvent welded into the small end of the taper section, and the other end of the pipe was cemented into the 2-inch side of the reducer on the resonator section containing the stack. The completed resonator is shown in Figure 13.

Figure 13. Resonator with two thermocouples, stack, and heat exchanger installed.

3.2 THE HOT-SIDE HEAT EXCHANGER

A heat exchanger for placement at the hot end of the stack was created from copper mesh and tubing. Several 4-inch diameter circles of copper mesh were cut from a sheet and soldered together to increase the surface area in contact with the working gas. In theory, the axial length of the hot-side heat exchanger should be twice the acoustic displacement amplitude of the gas so that even gas parcels that only contact the stack at their maximum excursion can expel the gained heat at their maximum displacement away from the stack [18]. The heat exchanger made for this project was limited by the method used for its manufacture. It was desired to keep the mesh circles aligned exactly behind one another; however, due to the somewhat low quality of the mesh and the difficulty in properly soldering the layers together, each added layer blocked a little more of the open area in the previous layers of mesh. To keep the heat exchanger from blocking too much of the resonator cross-section, fewer layers were added than were required to achieve an axial length of twice the gas displacement. The effect was that not all of the gas in contact with the stack could properly reject heat to the exchanger, so more of the acoustic power supplied to the resonator was wasted than would have been if the heat exchanger were the proper length; however, a shorter heat exchanger results in less viscous loss as there is a smaller surface area.

After soldering the mesh together, a coolant tube was added. The tubing was 0.125-inch outer diameter soft copper tubing. The copper tubing was bent into a serpentine pattern and soldered flat to the mesh. A few centimeters of tubing were left overhanging the mesh at either end of the pattern to allow the tubing to protrude through the resonator wall once installed. Two holes were drilled opposite each other in the resonator near the place where the hot end of the stack was to be. The copper mesh and tubing were flexible enough to bend and insert into the 4-

inch resonator section. Once the heat exchanger was flattened again, the holes in the resonator wall were sealed around the protruding tubing with epoxy resin. Then, plastic tubing was slid over the ends of the copper tubing to transport coolant to and from the resonator. The installed heat exchanger is shown in Figure 14.

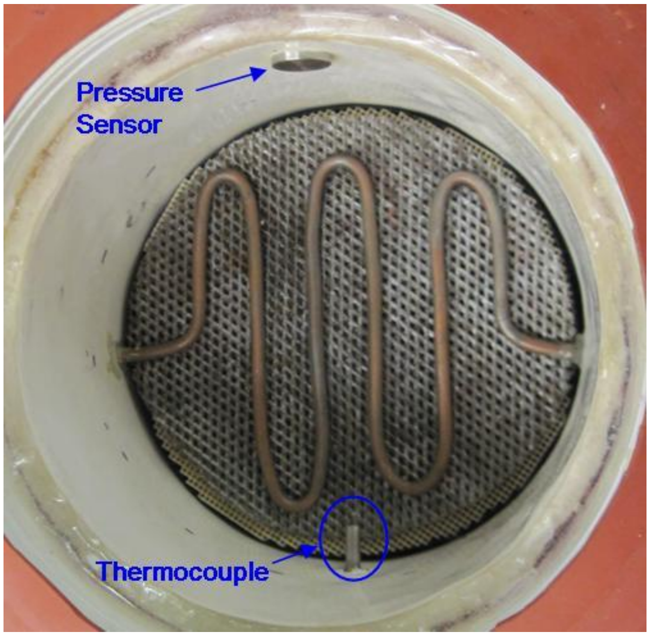

Figure 14. Heat exchanger, pressure sensor, and thermocouple installed.

3.3 THE SPEAKER BOX

A speaker box was made that could be bolted to the resonator in order to contain the working gas. Like the stack section of the resonator, the speaker box was made from a 4-inch diameter pipe. The pipe was cut to 15 cm in length and glued into a flange; the other end was capped. The basket of the speaker fit neatly into the box. Indentations were ground into the speaker flange to allow bolts through the PVC flange; this way, the bolts could be used to align the speaker face as well as clamp the speaker box to the resonator.

The final TAR was to be sealed, but access to the inside of the speaker box was desired for instrumentation. Independently sealing the speaker to its box would require resealing it every time the accelerometer or speaker leads needed an adjustment. Therefore, the speaker flange was simply sandwiched between the PVC flanges of the speaker box and resonator, using gaskets to create a seal (see Figure 15). Input wires for the speaker were soldered on the inside of the box to a BNC bulkhead feed-through. The wires could easily be detached from the speaker leads as necessary, allowing the speaker to be removed for access to the interior of the box.

Figure 15. TAR open at speaker face.

Finally, a gas port was added to the speaker box. Although the port was behind the speaker, gas could flow through the speaker cone. Assuming the resonator is not filled quickly, this method of charging does not damage the speaker. A hole was drilled and tapped near the back end of the speaker box to accept a 0.25-inch NPT pipe nipple. A valve was attached to the nipple and fitted with a 0.25-inch NPT to 0.375-inch flare coupling. Flare couplings are used with charging manifolds and hoses, which were used to fill the TAR with helium. All of the NPT junctions were sealed with polytetrafluoroethylene (PTFE) Thread Seal Tape; flare fittings do not require any sealant. The completed speaker box is shown in Figure 16.

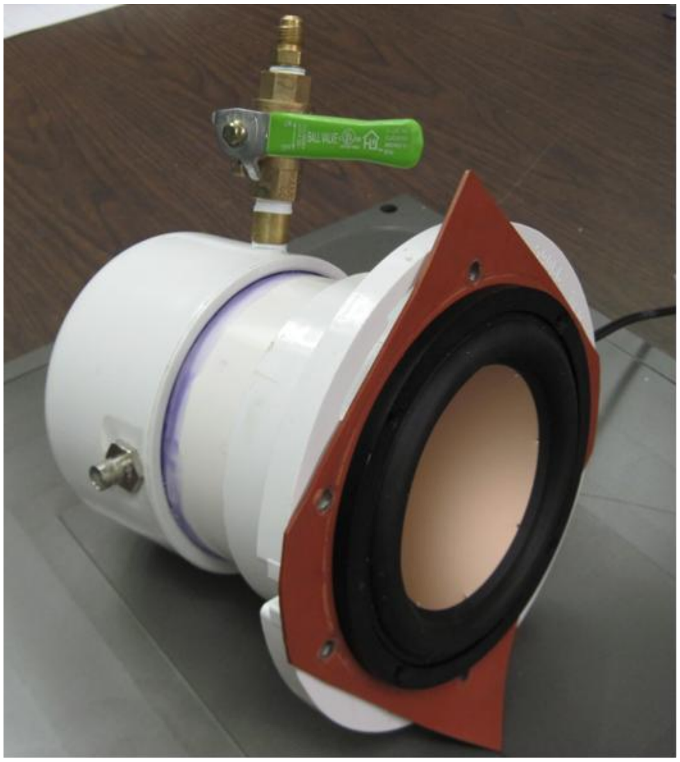

Figure 16. Speaker box with accelerometer feed-through, gas port, speaker, and input feed-through (rear) installed.

3.4 INSTRUMENTATION

Use of the various control schemes required the measurement of acceleration and pressure at the face of the driver (see Section 4.0). Other measurements of interest are the hot- and cold-side temperatures within the resonator. Appropriate sensors were mounted on the speaker and resonator wall to take the desired measurements.

The speaker acceleration was measured using a PCB 352C22 shear accelerometer. Its sensitivity was 9.53 mV/g over a range of 1-10,000 Hz. It was mounted to the back of the speaker face with Loctite® Super Glue Control™ Gel as shown in Figure 17. The lead from the accelerometer was attached to a 10-32 threaded to BNC bulkhead feed-through. There was enough slack in the wire that it did not impede the movement of the speaker cone.

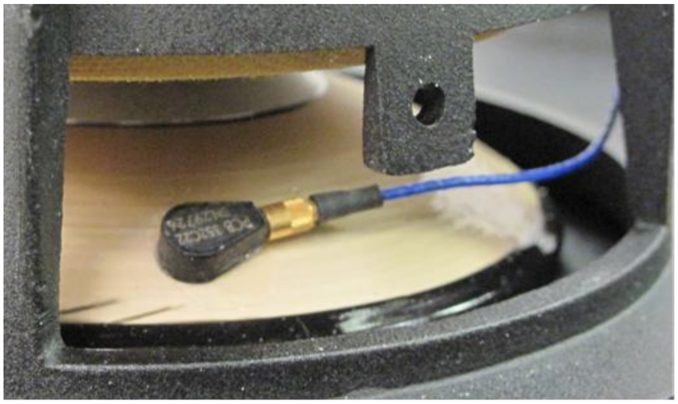

Figure 17. Accelerometer mounted to back of speaker cone.

Pressure was taken via a PCB 116B02 pressure sensor. Its sensitivity was 0.9310 pC/kPa with a measurement range of 689.5 kPa and maximum static pressure of 20.685 MPa. The sensor was flush mounted through the side of the resonator as close to the speaker face as possible without badly degrading the integrity of the PVC flange on the resonator (see Figure 14). The mounting specifications required that an extra piece of PVC be added to the exterior of the resonator to create the necessary wall thickness. A hole was appropriately drilled and tapped and the sensor inserted so that its output remained on the exterior of the resonator.

Two similar thermocouples were used to measure the hot- and cold-side temperatures at the ends of the stack. They were Omega TC-T-1/8NPT-E-72 thermocouples, which are type T exposed junction thermocouples for use in pipes. The outputs from the thermocouples were read by Omega MDSSi8 Series Benchtop Indicators. The thermocouples were mounted as close to the ends of the stack as possible by drilling and tapping holes to receive 0.125-inch NPT threads, which were sealed with the same seal tape as before. The thermocouples allow the calculation of the heat flow from conduction down the temperature gradient in the stack, $\dot{Q}_S$, as well as the heat flow from the environment to the cold side of the resonator, $\dot{Q}_{CHX}$, provided environmental temperature is known. These quantities combined with the applied acoustic power, $\dot{W}$, which can be calculated, yield the cooling power of the thermoacoustic process by

$$\dot{Q}_C = \dot{Q}_S + \dot{Q}_{CHX} + \dot{W} \, . \tag{65}$$

To clarify, Equation (65) gives the total heat that is pumped from the cold end of the stack to the hot end. In most cases, it is simply the heat flow from the cold-side heat exchanger (useful heat pumping) that is of interest in calculations of a TAR’s thermodynamic efficiency.

4.0 CONTROL OF THE THERMOACOUSTIC REFRIGERATOR

Several types of control have been used to facilitate the thermoacoustic process in TARs, including lock-in amplifiers [22, 24], extremum-seeking control [44], and a form of “sensorless” control [45]. The general idea is to drive the resonator at or near its fundamental acoustic resonant frequency. Assuming the device is perfectly designed (i.e., the resonator and driver have precisely the same resonant frequency), this frequency will produce the most acoustic pressure and the best phasing for creating a large thermoacoustic effect. One may use a signal analyzer to find the resonant frequency of the system and run the driver at that frequency throughout operation, which works reasonably well for systems with a moderate degree of damping so that performance does not degrade with small variations in frequency; but because a desirable acoustic resonator has low damping, the peak is usually relatively narrow and the driving frequency must then be more accurate. Furthermore, the speed of sound is highly dependent on temperature, so the actual resonant frequency of the system can change considerably throughout operation of the TAR [20], due to, for example, variations in heat load or environmental temperature. Therefore, it is desirable to implement a controller to ensure that the changing resonant frequency of the system can be tracked. Also, if TARs are ever produced on a large scale, there will be tolerances involved, and the resulting TARs may not have perfectly matched drivers and resonators; then, the optimum operating frequency may not be the fundamental acoustic resonant frequency. In this case, it would be important to know whether controlling a different parameter, say acoustic pressure or power transfer, would result in better performance. For this reason, three methods of control were investigated. The first method was a phase-locked loop (PLL), which is the standard way to control TARs [22, 24]; the second and third methods were a gradient ascent algorithm applied to pressure at the speaker face and the same algorithm applied to acoustic power transfer from the driver, respectively.

The extremum-seeking control [44] mentioned above was similar to a gradient ascent approach except the step size in the former was fixed and it operated on electroacoustic efficiency. In contrast, the gradient ascent algorithm presented here incorporated an adaptive step size (see Section 4.2) and was applied to other parameters.

One should note that, as discussed in Section 2.4, the optimum stack parameters are dependent on frequency, but these parameters cannot easily be manipulated during operation. The inability to manipulate the parameters may seem like a problem, but it turns out that for two reasons the actual effect of the varying frequency is small where stack parameters are concerned. First, the effective placement of the stack in the standing wave will change while the TAR is running; however, because the frequency is sufficiently high, a change in frequency of a few hertz will not greatly affect the wavelength of the sound. Therefore, the position of the stack in the standing wave will not change appreciably during the course of operation. Second, consider the spacing in the stack. The changing temperature will affect the optimum spacing, but a practical refrigerator would be designed to sustain a certain temperature so that the stack spacing can be designed with that temperature in mind. Although the spacing will not always be optimal, it will be very close the majority of the time. Because the effects of temperature on stack parameters are fairly small, methods of varying the stack length, position, and pore size would not be worth the added complication—especially considering that mechanical simplicity is one of the attractive features of TARs.

4.1 PHASE-LOCKED LOOP

One way to lock on to the acoustic resonant frequency is to lock on to the phase at that frequency, which can be done with a phase-locked loop (PLL) [46]. This method is reasonably effective because a large change in phase response occurs near resonance when a system is lightly damped, as is the case with most acoustic ducts. In the neighborhood of resonance, the frequency changes very little with respect to phase; that is, a small error in phase yields a much smaller error in frequency. Therefore, if the controller maintains the phase of resonance, the resonance frequency is also maintained.

In the case of an acoustic duct, the phase between pressure and particle velocity at the driver is the quantity of interest. This phase should be approximately 0° at resonance for a quarter-wave resonator [40, 47]. At first, this may seem counter intuitive as the phase in a pure standing wave is 90°, but the acoustic field within the resonator of a TAR actually consists of both a standing wave and a traveling wave because there is some acoustic power transfer. To show this, imagine the resonator as a circular pipe with length L and cross-sectional area S driven by a piston at $x = 0$ and open at $x = L$. The piston imposes sinusoidal motion at a frequency, ω, below the cutoff frequency of the first nonplanar mode, so only plane waves propagate; that is $\omega < \omega_{1,1} = 1.84a / R$ [40], where a is again the adiabatic speed of sound and R is the radius of the duct. The pressure and particle velocity in the pipe are given by [40]

$$p = Ae^{j(\omega t - kx)} + Be^{j(\omega t + kx)} \tag{66}$$

and

$$u = -\frac{1}{\rho_0}\int \frac{\partial p}{\partial x} dt\ , \tag{67}$$

where A and B are the amplitudes of the pressure waves traveling in the positive and negative x directions respectively. The mechanical impedance of the wave, Z_m, at the ends of the pipe must satisfy the boundary conditions due to the continuities of force and particle speed. Before moving on, perfectly lossless propagation of sound is assumed so that the propagation constant is purely real. Defined by the complex ratio of pressure over particle velocity, the impedances Z_{m0} and Z_{mL}, at $x = 0$ and $x = L$ respectively, can be written as

$$Z_{m0} = \rho_0 aS \frac{A + B}{A - B} \tag{68}$$

and

$$Z_{mL} = \rho_0 aS \frac{Ae^{-jkL} + Be^{jkL}}{Ae^{-jkL} - B^{jkL}} \quad . \tag{69}$$

Eliminating A and B by combining Equations (68) and (69) yields

$$\frac{Z_{m0}}{\rho_0 aS} = \frac{Z_{mL} + j\rho_0 aS \tan kL}{\rho_0 aS + jZ_{mL} \tan kL} . \tag{70}$$

Now, assuming the open end of the pipe is an ideal pressure node, the mechanical impedance there will be zero. The input impedance then reduces to

$$\frac{Z_{m0}}{\rho_0 aS} = j \tan kL\ . \tag{71}$$

Notice that the mechanical input impedance is purely imaginary, implying that the phase between pressure and particle velocity will be 90° for all frequencies, including the first resonance frequency.

Now, assuming there is some dissipation of energy in the acoustic medium, one must have a complex wave number, *k'*, defined by

$$k' = k - j\alpha\,, \tag{72}$$

where α is the absorption coefficient of the oscillating fluid. Omitting the derivation as it is much the same as before, the new expression for the input impedance of the pipe is

$$\frac{Z_{m0}}{\rho_0 aS} = \frac{1 + j\,{}^{\alpha}\!/_{k}}{1 + {}^{\alpha^2}\!/_{k^2}} \frac{\sinh\alpha L \cosh\alpha L + j\sin kL\cos kL}{\cos^2 kL\cosh^2\alpha L + \sin^2 kL\sinh^2\alpha L}\,. \tag{73}$$

The input impedance is complex, and its phase depends on frequency. If α is sufficiently small, some simplifying assumptions can be made. For helium, $\alpha / f^{\,2} \approx 1.87\times 10^{-11}$ (Np·s^2/m) [40], where α is in nepers per meter (Np/m) and f is the oscillation frequency in hertz (Hz). Therefore, one can assume $\alpha / k << 1$ and $\alpha L << 1$. The phase angle introduced by the α/k terms, which is $\tan^{-1}(\alpha / k)$, can then be neglected with no significant loss of accuracy [40]. Furthermore, the expression for input impedance can be simplified to

$$\frac{Z_{m0}}{\rho_0 aS} = \frac{\alpha L + j\sin kL\cos kL}{\cos^2 kL + (\alpha L)^2\sin^2 kL}\,. \tag{74}$$

The real and imaginary parts of the input impedance, R_{m0} and X_{m0}, are shown in Figure 18 with $\alpha L = 0.1$. When α is zero, Equation (74) reduces to Equation (71), and the plot for X_{m0} becomes asymptotic at $kL = \pi/2$. Intuitively, the effect of a nonzero α is that the reactance becomes bounded and switches from positive to negative quickly in the neighborhood of resonance. Resonance and antiresonance occur when the reactance, X_{m0}, vanishes. It is apparent that the first resonance occurs near $kL = \pi/2$, which agrees with the pipe being a quarter-wave resonator. Furthermore, with a nonzero α, the phase angle of the input impedance becomes 0° at resonance, which implies that the pressure and particle velocity are in phase at the face of the driver.

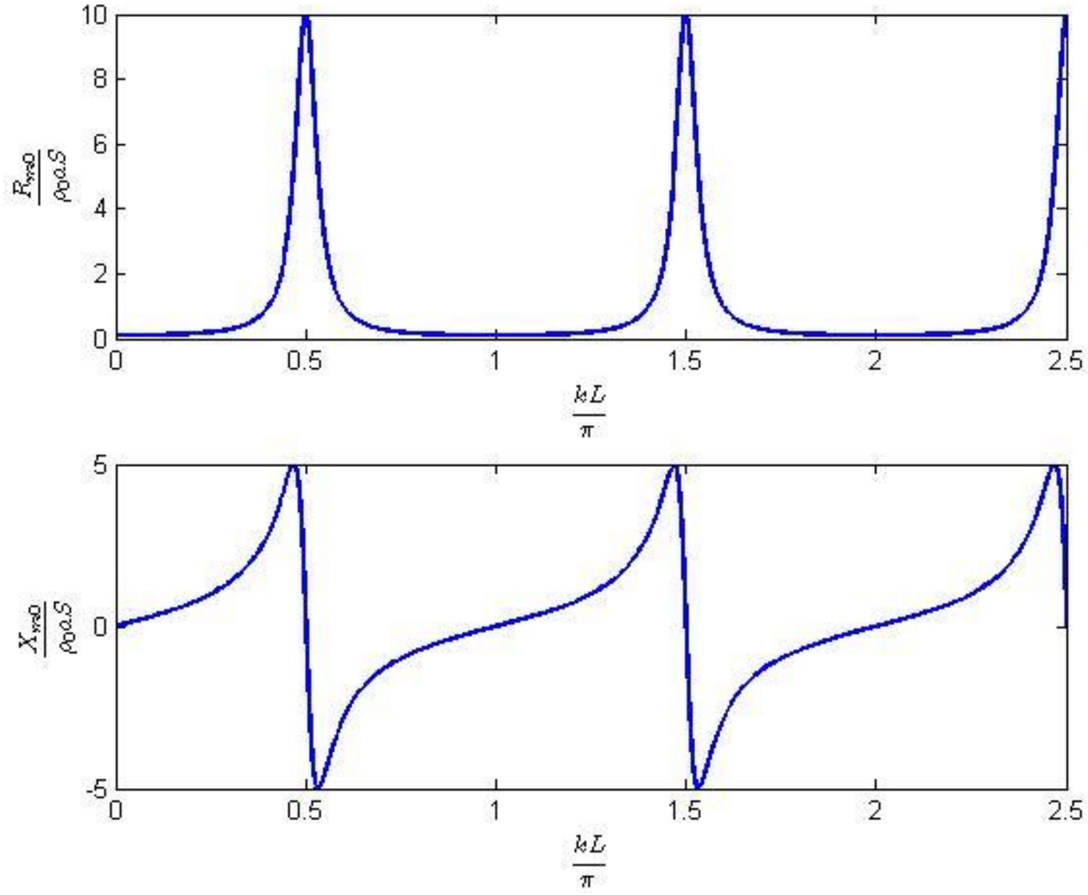

Figure 18. Real and imaginary parts of input impedance for a driven-open tube of length L with $\alpha L = 0.1$.

With a known target phase, a PLL can be implemented. PLLs comprise a phase detector, a loop filter, and a voltage-controlled oscillator (VCO) as shown in Figure 19. The phase detector outputs a signal “proportional” to the difference in phase between the reference signal, *r*, and the output signal, y; the loop filter tunes the dynamics of the control loop to desired parameters; and the VCO outputs an oscillating signal at a frequency determined by the conditioned signal from the phase detector. The control loop functions such that the VCO output is adjusted to the desired frequency and phase relative to the input [46].

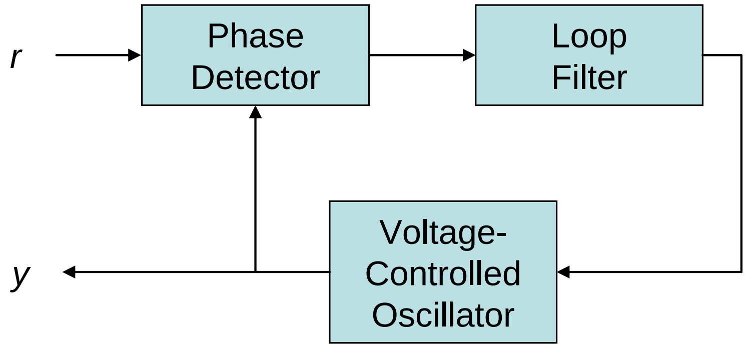

Figure 19. Schematic of a phase-locked loop.

When tracking a resonant frequency of a system, the output from the PLL is used as the input to the plant and an appropriate system output must be chosen for use as the reference signal. As discussed above, the desired phase between particle velocity and pressure is known, so these two signals would be useful as inputs to the phase detector. Unfortunately, particle velocity can be somewhat difficult to measure directly; acceleration, however, is easy to measure and has a known phase relationship with velocity—velocity lags behind acceleration by 90°. The desired phase of pressure relative to acceleration at the driver face is then -90°. Note that in the setup of a standing-wave TAR, the acceleration of the driver can be viewed as an input to the acoustic duct, and the pressure at the face of the driver can be viewed as an output. These two signals are appropriate inputs for the PLL controller. The phase detector was implemented as a multiplier; a signum function, a Butterworth low-pass filter (LPF), and an integrator were used in the loop filter; and the VCO was made to operate so that a constant voltage input would drive a constant frequency output. The controller is shown in Figure 20 as modeled in Simulink™.

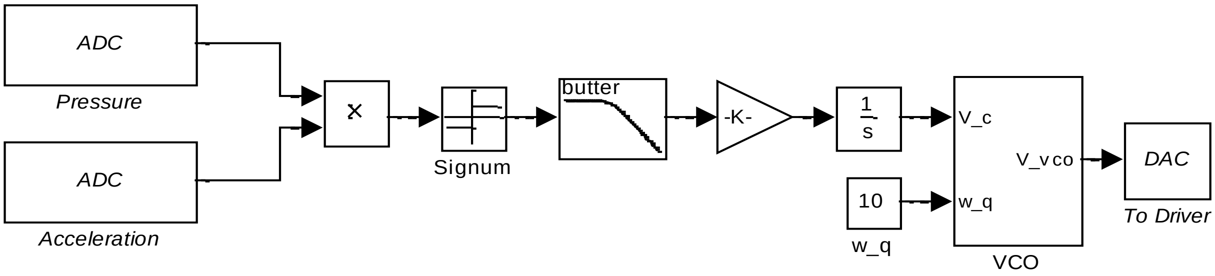

Figure 20. Simulink™ model of the PLL controller as implemented on the TAR.

For this work, a simple multiplier was used as a phase detector. This method of phase detection takes advantage of trigonometric identities to output a suitable signal. The pressure sensor and accelerometer signals that will be used as inputs to the multiplier are sinusoids with some error in phase difference, φ. The two signals can be written as

$$V_p = A_p \sin(\omega_p t) \tag{75}$$

and

$$V_a = A_a \cos(\omega_a t + \varphi), \tag{76}$$

where the subscripts p and a refer to the pressure and acceleration signals respectively; and V is the instantaneous voltage, A is the amplitude, and ω is the frequency of the indicated signal. The output of the multiplier can then be expressed as

$$V_a V_p = \frac{A_a A_p}{2}\left[\sin\left(\left(\omega_p - \omega_a\right)\cdot t - \varphi\right) + \sin\left(\left(\omega_a + \omega_p\right)\cdot t + \varphi\right)\right] \tag{77}$$

so the first term is a sinusoid with a frequency that is the difference between the input frequencies, ω_p and ω_a, and the second term has a frequency equal to the sum of the input frequencies. To extract the phase difference information, the input frequencies must be the same. Fortunately, many dynamic systems, including the resonator in the present work, respond at the frequency of excitation, making $\omega_p = \omega_a = \omega$. Equation (77) then reduces to

$$V_a V_p = \frac{A_a A_p}{2}\left[\sin(-\varphi) + \sin(2\omega t + \varphi)\right]. \tag{78}$$

The multiplier output is then the sum of a DC bias signal and a double frequency signal. The total output from the phase detector contains the phase information, but it must be conditioned to become an appropriate input to the VCO.

The loop filter extracts the necessary information by attenuating the double frequency term and modifies the dynamics of the control loop. For the present work, the loop filter had two stages. The first component was a signum function, which outputs a signal with unit magnitude while preserving the sign of the input. In essence, the signum output is a pulse-width modulated signal where the on state is 1, the off state is -1, and the duty fraction (DF) increases with the bias in the multiplier output. An example comparison between a multiplier output, y_1, for $\varphi = -\pi/6$ and the corresponding signum output, y_2, is illustrated in Figure 21. The zeros of y_1 determine the DF of y_2. The DF of a signum function's output when its input is given by Equation (78) was found to be

$$DF = {}^{1}\!/_{2} - {}^{\varphi}\!/_{\pi}. \tag{79}$$

Equation (79) shows that the DF of the signum output is an affine function of the phase error between the pressure and acceleration signals and is independent of their magnitudes. Magnitude independence is advantageous because it allows the control loop to function based on the phase response of the system alone. Otherwise, the small magnitude response away from resonance would result in a much smaller control signal and, therefore, a much longer lock-on time. Furthermore, the large magnitudes near resonance would tend to create a larger oscillating error around the lock-on frequency. These magnitude effects play an especially strong role when the plant being controlled is lightly damped as is the case with most TARs, so the effects of the signum function are more desirable in such instances.

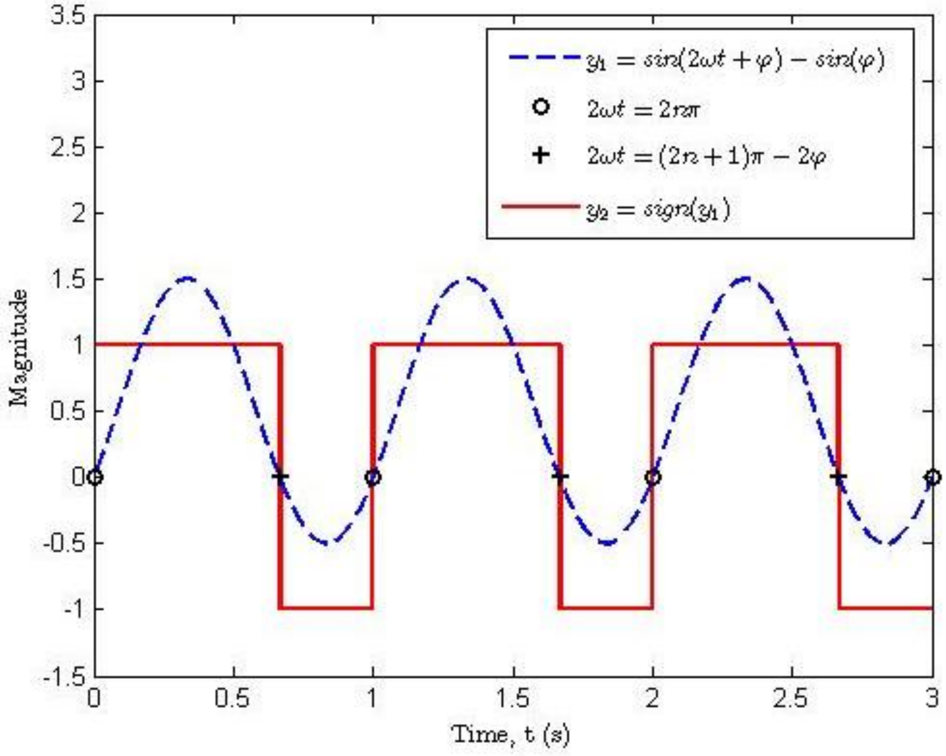

Figure 21. Effect of a sigmoid function on the multiplier output.

The output of the signum function was then filtered by a Butterworth LPF and an integrator in the second stage of the loop filter to improve the performance of the controlled system. Although a PLL control loop can function without a Butterworth LPF (the integrator is also an LPF), the addition of the Butterworth filter allows improvement of both lock-on time and steady-state oscillating error. Lock-on time decreases linearly with increasing integral gain whereas the amplitude of the oscillating error increases linearly with integral gain, so if simplicity is paramount, an acceptable compromise may be achievable; however, by adding a second-order Butterworth LPF, the double frequency part of the control signal, which is the source of the oscillating error, can be attenuated without adversely affecting the lock-on time of the controller [46].

Finally, the loop filter output is used as the control signal for a VCO. The VCO outputs a constant amplitude signal at a frequency that is proportional to the sum of the control signal and a constant, known as the quiescent frequency. The quiescent frequency is an initial guess at the acoustic resonant frequency. From there, the PLL provides the VCO with a command signal that increases or decreases the frequency until an equilibrium point is found. At that point, the time-averaged input to the integrator and, by extension, the loop filter must be zero. Therefore, the controlled system drives itself to a state where $\varphi = 0$, as is evident in Equation (78), and the operating frequency thus tracks the changing resonant frequency.

4.2 GRADIENT ASCENT CONTROL

A gradient ascent algorithm was developed and applied to each of two operating parameters, pressure and acoustic power transfer, to maximize those values. While PLLs ensure that the desired acoustic resonance is tracked, they do not ensure that the driver creates the maximum achievable dynamic pressure or that the driver transfers the greatest possible acoustic power to the resonator and thermoacoustic core. Both maximum acoustic pressure and maximum acoustic power transfer are desirable to achieve good performance from the TAR, but as stated previously, the optimum frequencies for maximizing each of these parameters may differ from each other as well as the acoustic resonant frequency. Therefore, controlling the driving frequency based on pressure or power transfer may yield better performance than the traditional PLL control.

To locate and track a maximum of some parameter, gradient ascent control can be implemented [48]. The basic idea is that there is some possibly unknown performance surface, and by estimating the gradient of this surface, the controller can change the independent variables to move the operating point in the direction of the gradient, eventually arriving and staying within some neighborhood of the maximum. When maximizing performance by changing one independent variable, the performance surface reduces to a performance curve

At this point, the algorithm will be described in terms of maximizing pressure with respect to frequency so that the physical significance of the algorithm is understood. In this case, the performance curve (shown in Figure 22) is defined by the root-mean-squared (RMS) pressure, p_{rms} (Pa), as a function of operating frequency, ω (rad/s).

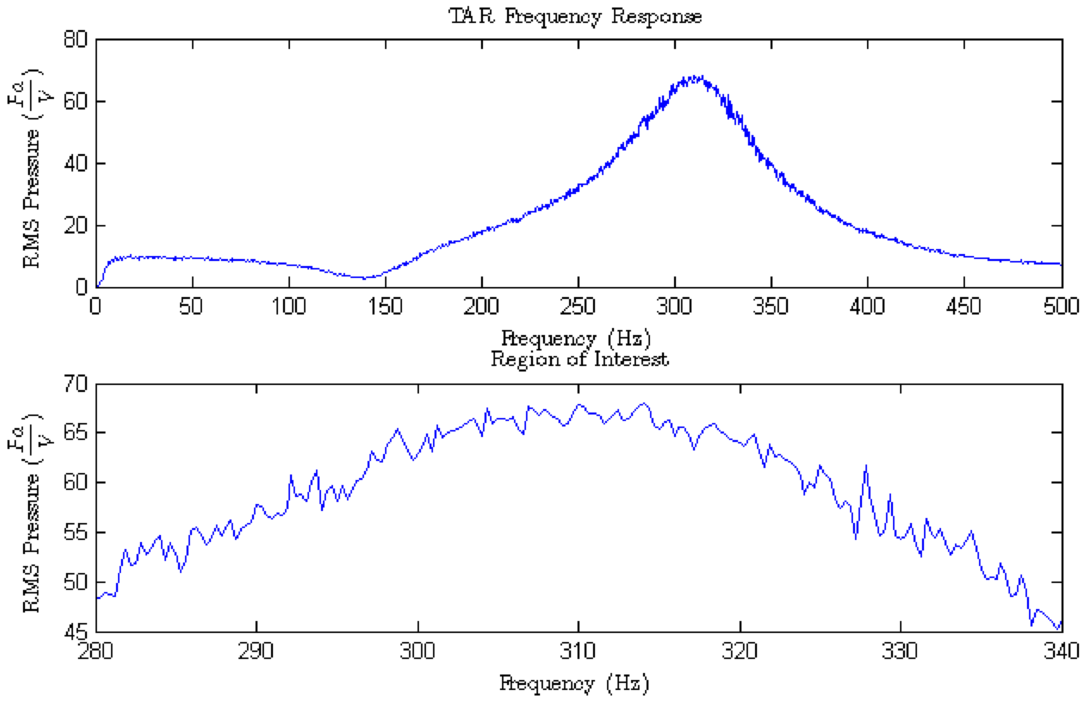

Figure 22. Performance curve for RMS pressure gradient ascent.

A starting frequency is chosen as a guess at the frequency corresponding to maximum pressure, and p_{rms} is measured. The measurement is taken at the end of a 5 second interval of operation so that any transient response has died out. The steady-state p_{rms} is then calculated by the last 10,000 samples (at 20 kHz) of the analog pressure signal, removing any linear trend, and taking the square root of the mean of the element-wise square of the vector. Thus, p_{rms} is a discrete signal with a period of several seconds. At the next time step, the controller increases the operating frequency by $\Delta\omega$, and another measurement is taken. The gradient is estimated as

$$\nabla p_{rms} \approx \frac{(p_{rms})_k - (p_{rms})_{k-1}}{\Delta\omega}, \tag{80}$$

where k is the time step. In the following time step, the new frequency is given by [48]

$$\omega_{k+1} = \omega_k + \mu \nabla p_{rms}, \tag{81}$$

where μ is the adaptation coefficient. Then, the procedure repeats until ω_k remains in a neighborhood of the performance curve maximum, where the gradient is near zero. This maximum is not maintained with absolute precision because of the perturbations required to measure the gradient, but $\Delta\omega$ and μ are chosen so that the final neighborhood is desirably small. The Simulink™ model of this controller is shown in Figure 23. The implementation of the gradient ascent algorithm is shown in Figure 24.

Besides accuracy, the choices of $\Delta\omega$ and μ are also contingent on the speed of convergence and maintaining the stability of the system [48]. Theoretically, a smaller $\Delta\omega$ provides a more accurate gradient estimate; but considering noise in the performance measurement, if $\Delta\omega$ is too small, the gradient estimate will be dominated by noise, and the controller will be considerably less precise in finding the maximum. Furthermore, depending on the type of noise, the controller will also be inaccurate.

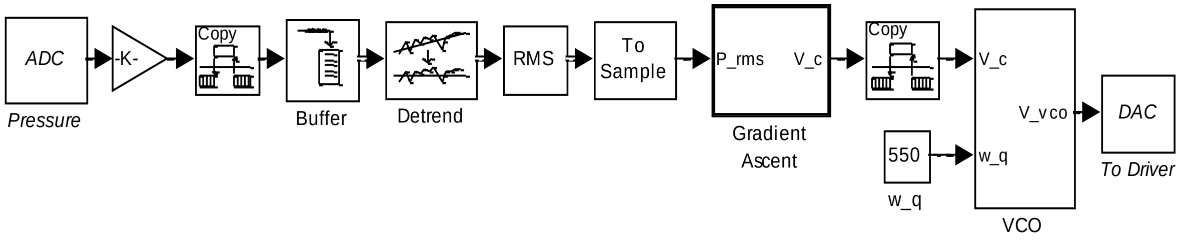

Figure 23. Simulink™ model of gradient ascent control applied to pressure.

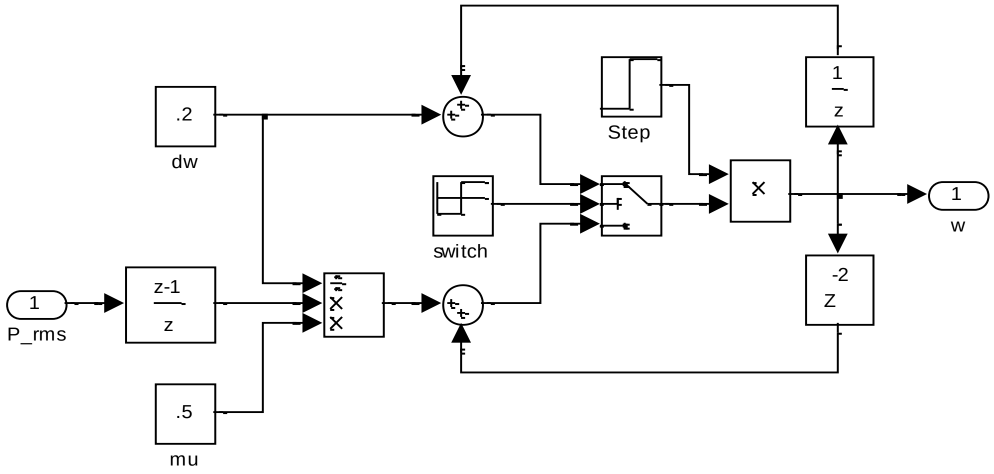

Figure 24. Simulink™ model of gradient ascent algorithm.

To choose an appropriate $\Delta\omega$, a 5th order polynomial was fit to actual pressure frequency response data within 10 Hz of the maximum. Then, the polynomial's Taylor series expansion was used to calculate the theoretical error of a first-order gradient approximation due to varying the size of $\Delta\omega$. Because the error is also dependent on the base point of the approximation, the error was averaged over several base points. The resulting error curve is shown in Figure 25. Another curve can be drawn for the error in the RMS measurement. After several trials, 95% confidence intervals were found for several frequencies of the RMS pressure measurement. Then the measurement error propagated through the gradient calculation was found to be

$$E_{meas} = \frac{2h_{CI}}{\Delta\omega}, \tag{82}$$

where h_{CI} is half of the confidence interval. This follows in a straight forward manner from the equation for the gradient estimate under the assumption that the confidence intervals for the unperturbed and perturbed frequencies, f_1 and f_2, are the same. This assumption is valid when $\Delta\omega$ is small enough that there is no rapid change in noise between f_1 and f_2. The total error can then be estimated as the sum of the truncation and measurement error estimates as shown in Figure 25.

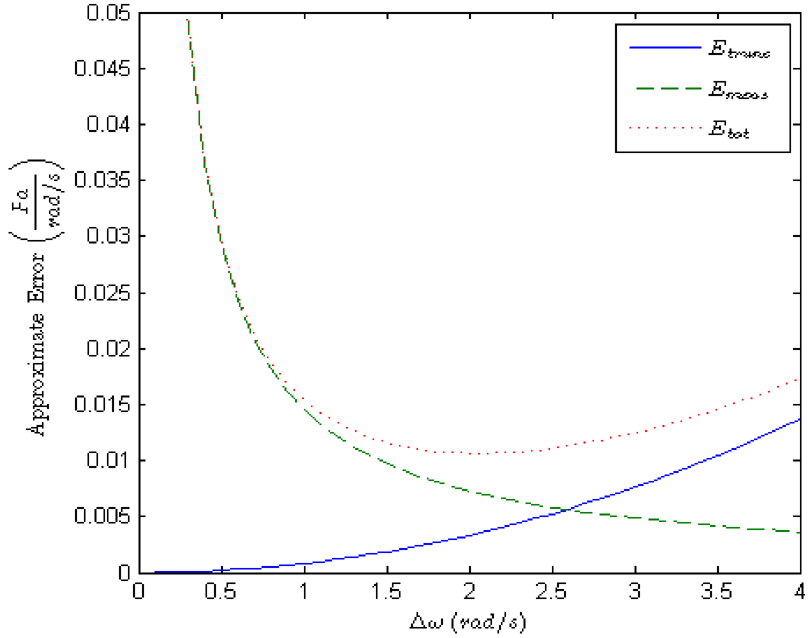

Figure 25. Plot of truncation error and measurement error of the gradient as a function of step size.

The minimum total error occurs at a perturbation step of $\Delta\omega$=2 rad/s, so that value was used as a starting point. The value of μ was chosen to be 0.5. Both of these values were based on approximations, so simulations were used to tune the two parameters using a system identification model taken from the real system before further tuning during experiments. Note that most gradient theory is based on a quadratic performance surface [48]. Because the performance surface is not quadratic and cannot be accurately approximated as quadratic, heuristic tuning methods were necessary.

The gradient ascent algorithm for maximum acoustic power transfer (shown in Figure 26) functioned in much the same way except for the performance criterion. It is important to note that power is a vector, so the RMS value could not be used; instead, the time averaged power defined the performance curve (shown in Figure 27).

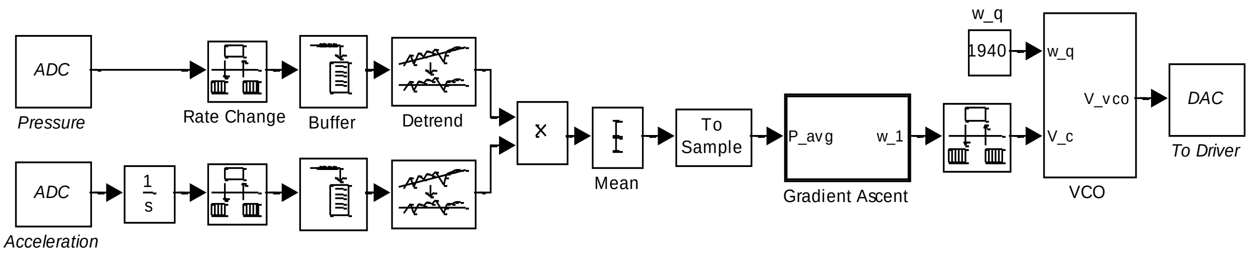

Figure 26. Simulink™ model of gradient ascent control applied to acoustic power.

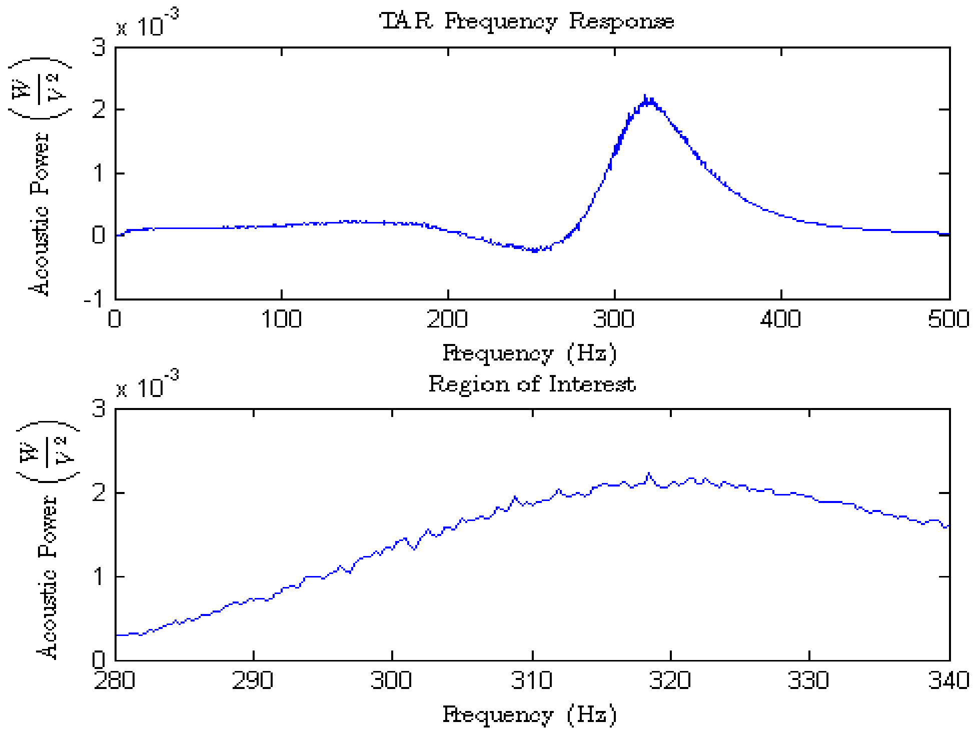

Figure 27. Performance curve for maximum power gradient ascent.

The time average of the instantaneous acoustic power flow per unit area, or intensity, is given by [49]

$$I = \frac{1}{T}\int_0^T p\vec{v}dt \ , \tag{83}$$

where T is the averaging period, p is acoustic pressure, and v is particle velocity. This expression for power flow is used because it is easier to measure pressure and velocity (the integral of acceleration) as real values on-line rather than as complex values, which can be used more easily off-line in analytical calculations. The pressure and velocity signals were multiplied and the resulting power signal was buffered as was the signal in the pressure controller. The mean of the buffered vector was then used in determining the gradient of power with respect to frequency. The same frequency update algorithm was used but with adjustments to μ and $\Delta\omega$. A similar error analysis was carried out for the new performance curve, but the resulting optimal $\Delta\omega$ was too large in that it would directly cause unacceptable steady-state precision. A suboptimal value of $\Delta\omega$=2 rad/s was chosen as the initial guess for experimentation. Again, the adaptive gain was chosen as μ=0.5, but both this parameter and the perturbation step were further tuned in simulations with a prediction error plant model and again in actual trials.

4.3 SYSTEM IDENTIFICATION AND SIMULATION

With models of the three controllers built in Simulink™, the next step was to simulate them with a plant model. An analytical model of a coupled speaker and duct system was first used as a model of the TAR, but it was difficult to find model parameters that fit the actual system well.

Therefore, system identification was used to create a model of the TAR, and that model was used for simulation. During simulation, the controllers' parameters were adjusted so that better performance could be expected during implementation on the real TAR.

The analytical model was based on independent models of a speaker and an acoustic duct that were then coupled through pressure at the speaker face. Using Smith [50] and Dickason [51] as guides, the speaker was defined as a state-space model with voltage and pressure as inputs and acceleration as an output. Smith [50] also provided a method for creating a state-space model for an acoustic duct with an acceleration input and two pressure outputs. One output was pressure at the speaker face, and the other was pressure at a sensor not necessarily collocated with the speaker. The two models were modified to represent the TAR, but choosing modal damping coefficients that accurately recreated the frequency response of the actual TAR was difficult. System identification was used as an alternate approach. A model was created with Matlab's System Identification Toolbox™. The data for the model were taken via Siglab. The frequency responses of pressure and acceleration at the speaker face due to a 1 Volt AC input were measured over a bandwidth of 0-500 Hz (shown in Figure 28). The data were then used to estimate the system parameters of a state-space model by a prediction error method. The resulting model was of the form

$$\begin{aligned} \dot{x} &= \mathbf{A}x + \mathbf{B}u + \mathbf{K}e(t) \\ y &= \mathbf{C}x + \mathbf{D}u + e(t) \end{aligned} , \tag{84}$$

where **A** is a 10x10 matrix, **B** is 10x1, **C** is 2x10, **D** and **K** are a zero vector and matrix, respectively; x, y, and u are state, output, and input vectors, respectively; and *e(t)* is prediction error. The initial states are assumed to be zero. The values of each matrix are given in Appendix B. The pressure frequency responses of the system and model are shown in Figure 29, and the acceleration responses are shown in Figure 30, where the measured data are represented by the solid blue lines, and the identified model is represented by the dashed red lines. The 10th order model showed very good agreement with the measured data.

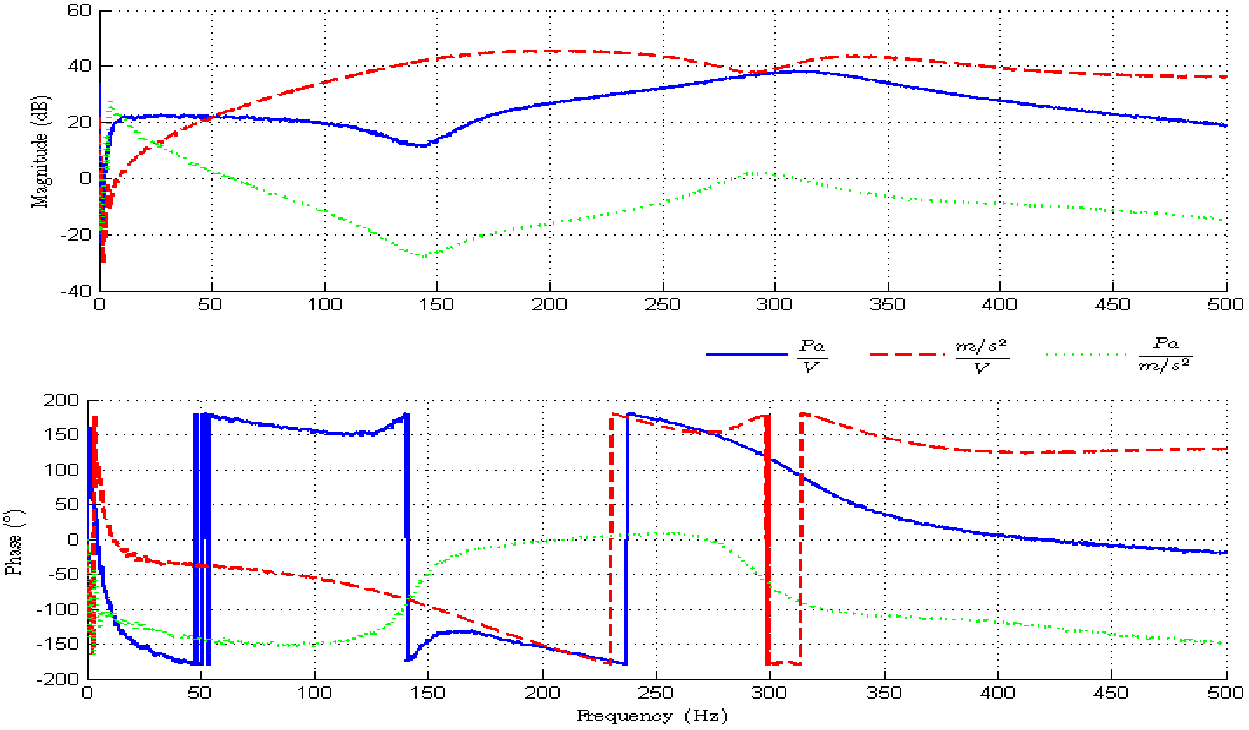

Figure 28. Frequency responses of TAR outputs and the transfer function from acceleration to pressure.

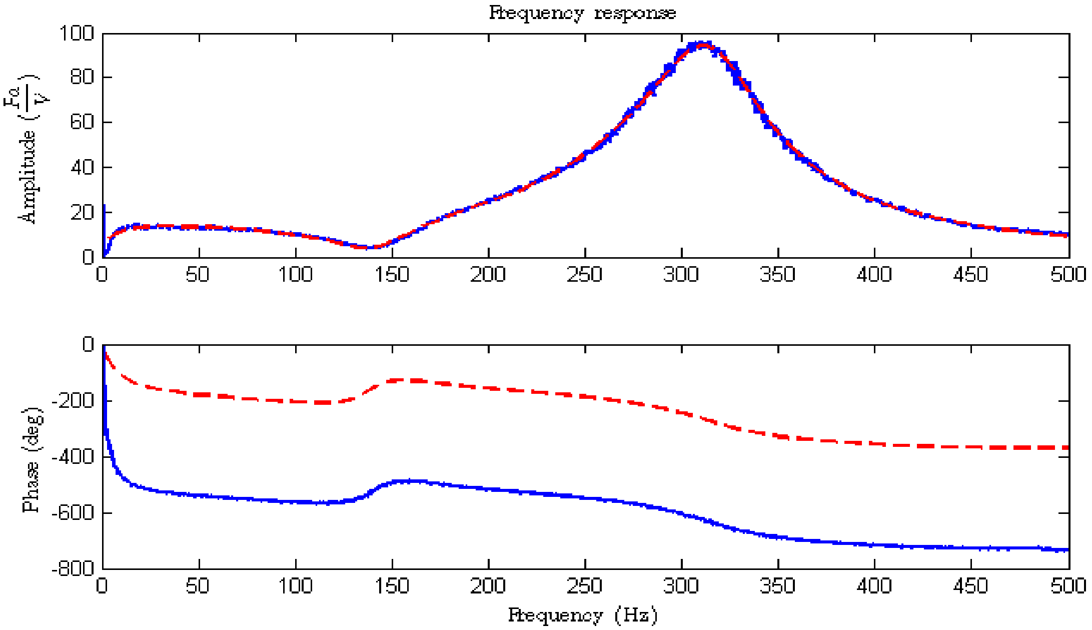

Figure 29. Comparison of pressure frequency responses of TAR and model.

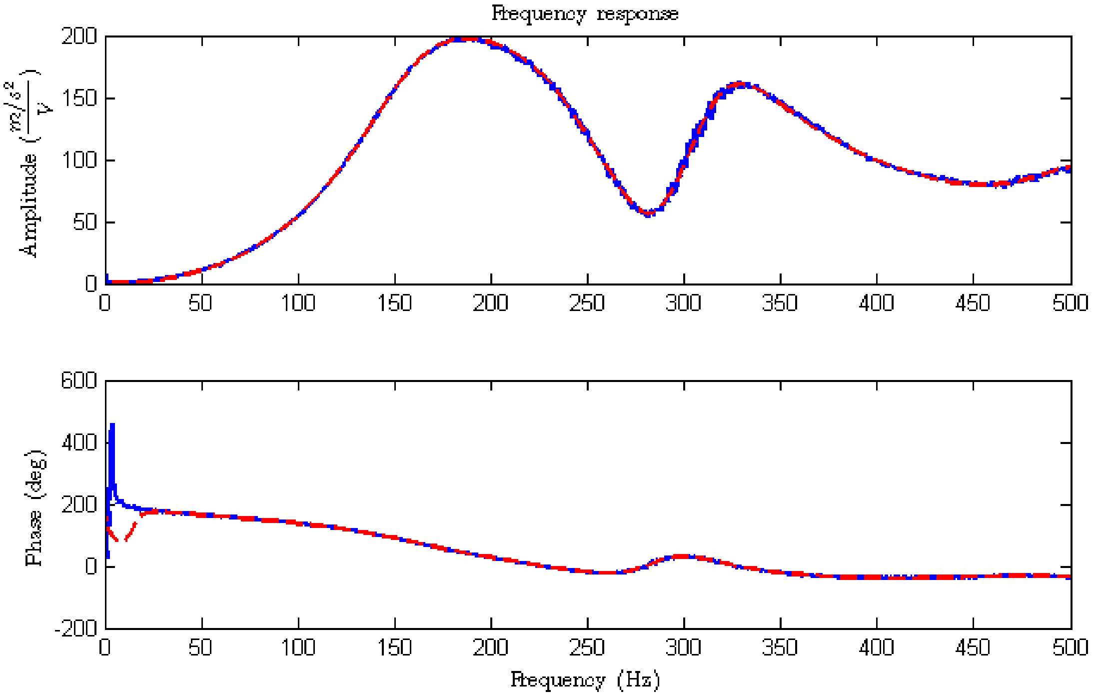

Figure 30. Comparison of acceleration frequency responses of TAR and model.

Next, each of the three controllers was applied to the identified model. The control parameters of each were changed until acceptable performance was achieved and a heuristic understanding of how each controller may act on the real system was obtained. Initially, each controller was started at 1850 rad/s and allowed to lock on to its optimum frequency. It was necessary to increase the perturbation step size of the gradient ascent controllers to 3 rad/s in order to obtain better gradient measurements. Because an increase was necessary, it is clear that the noise error calculations were not conservative. Also, it was found that μ could be much larger than anticipated and still yield a stable control loop, but the steady-state precision began to degrade around μ=50 for the pressure control and μ=60,000 for the power control.

As simulations continued, the PLL showed very fast (< 1 s) and precise (~±0.1 rad/s) lock-on characteristics, while the gradient ascent controllers were several orders of magnitude slower (~ minutes) and were less precise (~±2.5 rad/s). Typical simulation results are shown in Figures 31-33. However, the simulated performances do not mean that the PLL is a superior control scheme for TAR applications. As seen in Figure 28, the maximum pressure occurs at a frequency different from the acoustic resonance frequency, which is the peak of the transfer function between acceleration and pressure; maximum power transfer occurs at still another frequency (see Figure 27). Although the gradient ascent controllers may not perform as well in terms of convergence time and steady-state precision, their operating frequencies may be better in terms of cooling power or COP. To compare these quantities, each controller was used on the real TAR via a dSPACE1104 platform.

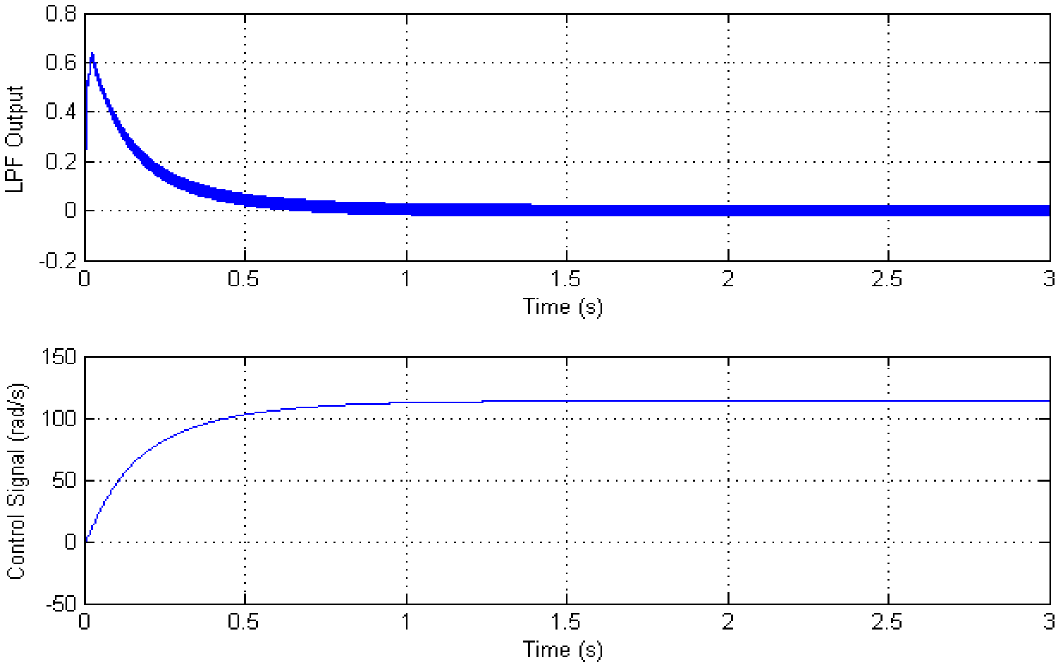

Figure 31. Typical simulation result for PLL control.

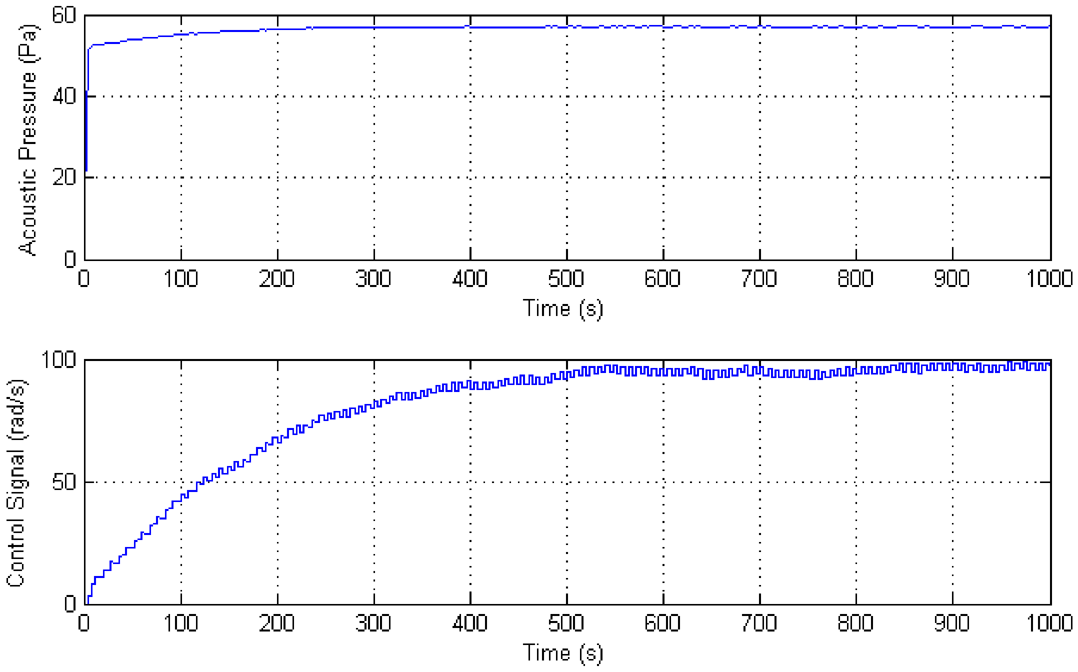

Figure 32. Typical simulation result for maximum pressure control with μ=40 and $\Delta\omega$=3 rad/s.

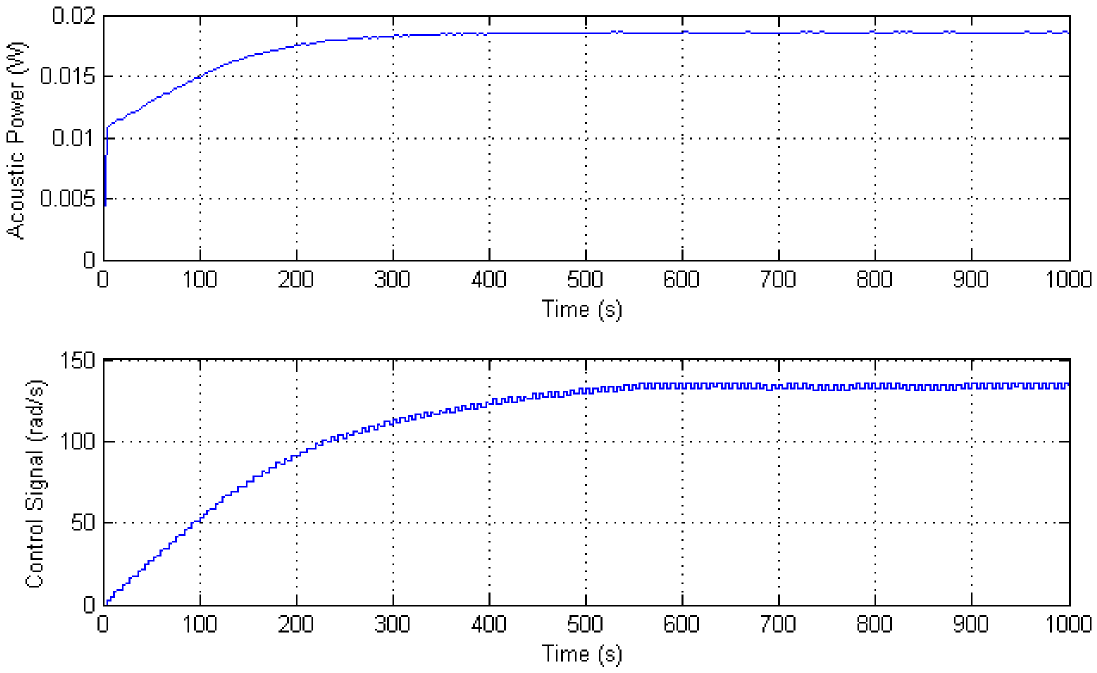

Figure 33. Typical simulation result for maximum acoustic power control with μ=50,000 and $\Delta\omega$=3 rad/s

5.0 RESULTS AND DISCUSSION

To assess the overall utility of each controller as applied to thermoacoustic refrigerators, several sets of data were collected for each and then condensed into more meaningful quantities, including steady-state temperature difference ΔT, average time to converge t_{conv}, steady-state precision ω_{spread}, steady-state cooling power $\dot{Q}_C$, and steady-state COP. Electrical power, Π_{elec}, and the electrothermal performance, $\mathrm{COP}_{\mathrm{elec}}$, of the overall device were also considered. The experiments were allowed to continue for several hours but were limited by the amount of available disk space. Typical results for the PLL and acoustic pressure controllers are shown in Figures 34 and 35, respectively. Difficulties in implementing the acoustic power controller on the dSPACE platform prevented the collection of enough data for a complete comparison to the first two controllers. The performance results are based on only one partially successful trial; that trial is shown in Figure 36.

Weeks of effort were spent on dozens of attempts to collect data for the acoustic power gradient ascent controller. Most attempts resulted in dSPACE errors or corrupt data files. Because of the many problems associated with collecting the data shown in Figure 36, it is difficult to say whether the control scheme was working properly. The downward drift at the end of the trial could be due to a flaw in the controller itself or a problem with the dSPACE board, or the acoustic power output of the speaker may be tracking a physical change in the system. Because the data were recorded after many trials, it seems probable that helium began leaking from the resonator. Leaking helium would have the effect of reducing the optimum frequency of the controller as shown in Figure 36. It is worth noting that the temperatures near the end of the trial are comparable to the temperatures of the other two controllers. However, because the differences between controllers are small, more data would need to be collected to enable thermodynamic comparison of the control schemes.

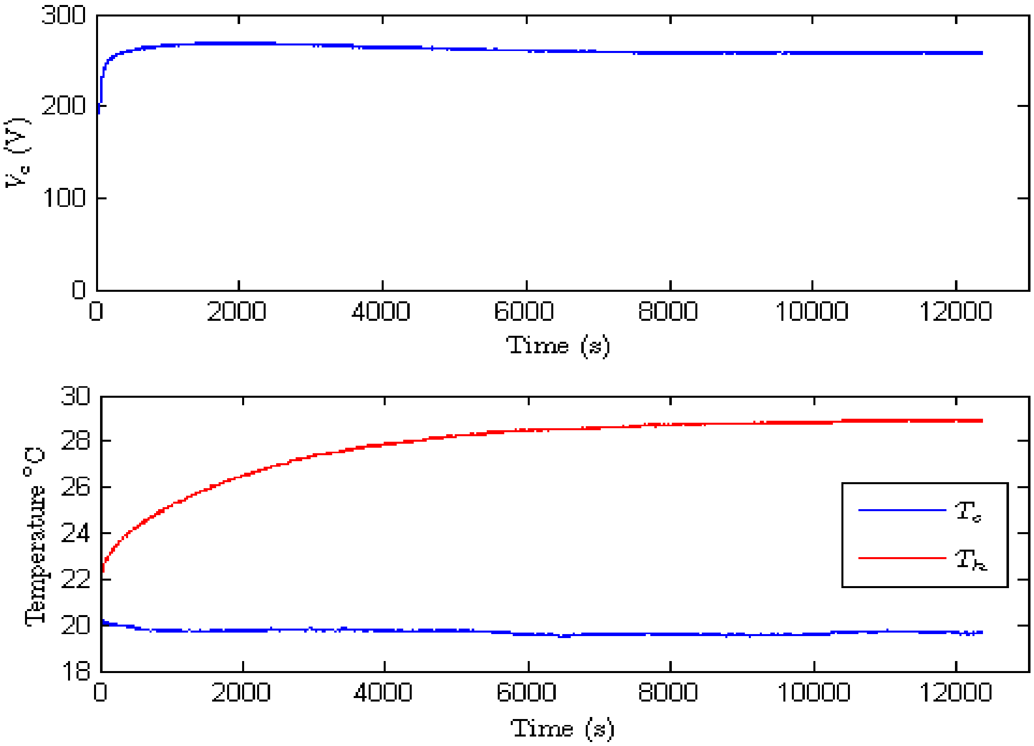

Figure 34. Typical results for PLL control.

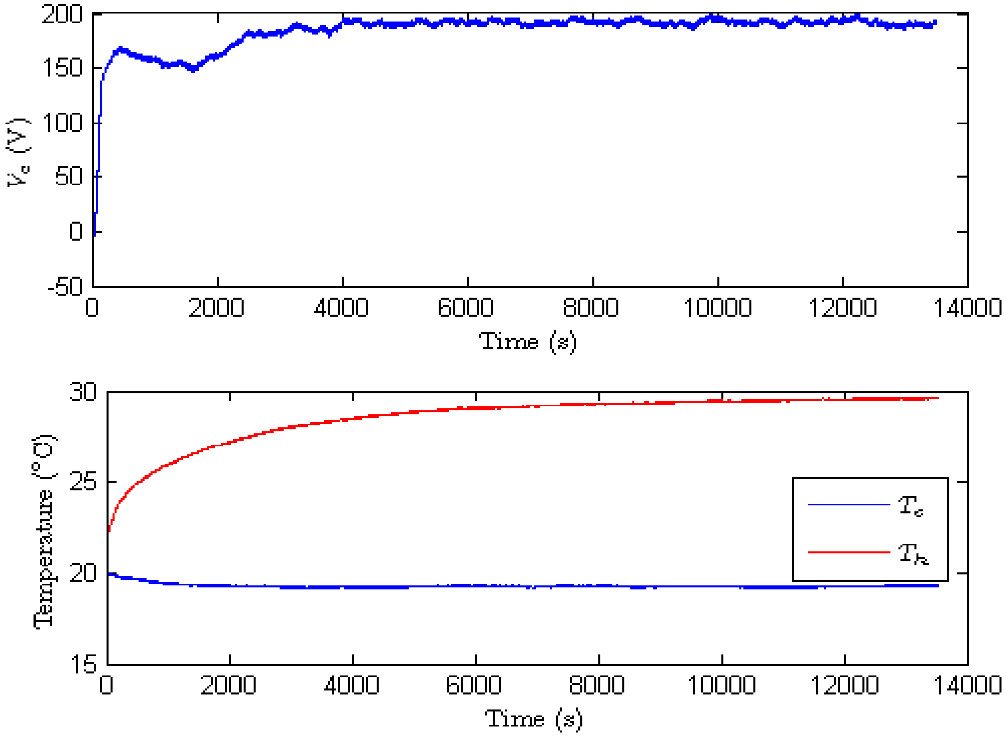

Figure 35. Typical results for acoustic pressure gradient ascent.

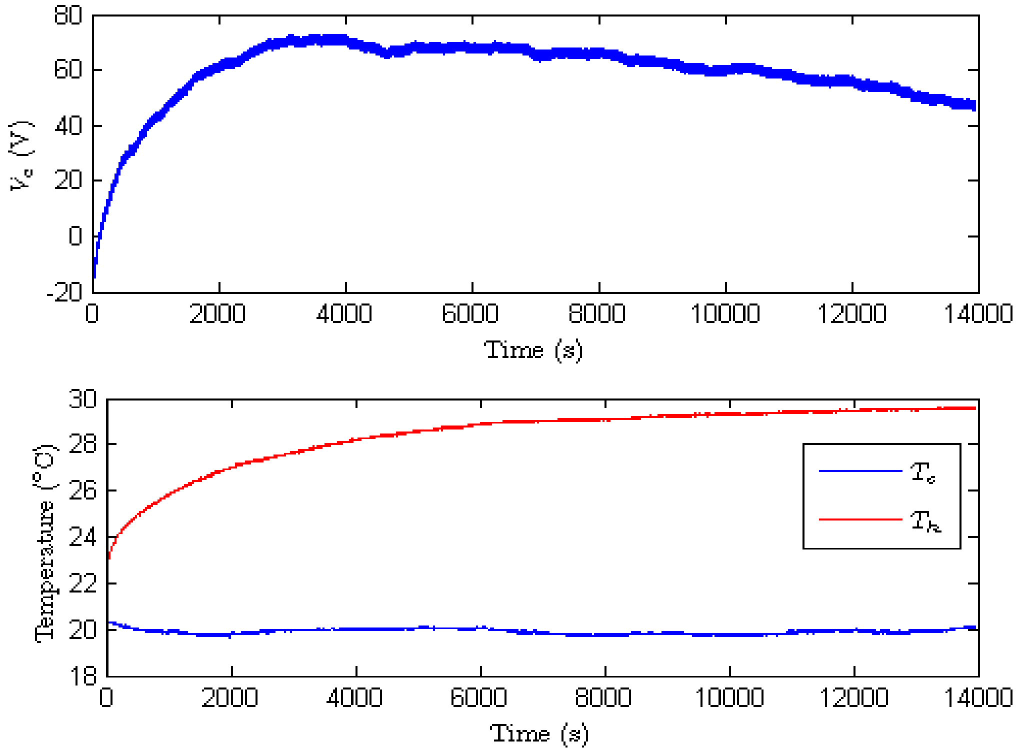

Figure 36. Results for acoustic power gradient ascent.

5.1 CONTROLLER PERFORMANCE

The control performance criteria were convergence time and steady-state precision, or spread. The convergence time was defined as the time it took the control signal to arrive and stay within the steady-state spread limits of its locked-on value. The spread was defined as the maximum excursion of the control signal from its locked-on value after the temperature difference across the stack had reached steady state. The values used to compare the control schemes were averaged over 5 trials for the PLL and pressure controls.

From a controls stand-point, the PLL far outperformed the acoustic pressure gradient ascent control. The results are summarized in Table 3. Even when starting more than 50 Hz from the acoustic resonance, the PLL converged within a few seconds. In addition, its average steady-state precision was better than ±1.5 rad/s. In contrast, the average convergence time of the pressure gradient ascent control was about 2500 s. The gradient ascent control was able to converge from a considerable distance away from its optimum frequency, but the lock-on times were unreasonably long; so, because the convergence was almost linear away from the optimum frequency, the gradient ascent experiments were limited to starting within 30 Hz of the lock-on frequency. Note that the linear convergence was coincidental and due to the nearly linear region of the performance curves. The steady-state precision of the pressure gradient ascent algorithm was reasonable at an average of about ±9 rad/s but could be improved by decreasing μ. However, as discussed earlier, decreasing μ is detrimental to lock-on time. Therefore, it is necessary to find an acceptable balance of convergence time and steady-state precision based on the constraints of a given application. Furthermore, faster algorithms could likely be found, but the purpose of this work was to demonstrate and compare control methods.

The acoustic power gradient ascent controller appeared to perform comparably to the pressure controller in terms of convergence time and steady-state precision. Quantitative comparisons were not warranted due to the lack of data. However, it is fair to say that the power controller converged much more slowly and had a larger ω_{spread} than the PLL due to the nature of the search algorithm.

Table 3. Comparison of control methods' experimental results.

Controller	t_{conv} (s)	ω_{spread} (rad/s)	ΔT (°C)	$\dot{Q}_C$ (W)	$\dot{W}$ (W)	COP	COPR (%)	Π_{elec} (W)	COP_{elec}	$COPR_{elec}$ (%)
PLL	1.2	1.5	9.64	10.76	2.445	4.40	14.19	24.76	0.434	1.43
Acoustic Pressure	2500	9.1	10.32	16.42	7.469	2.20	7.73	28.70	0.572	2.02

5.2 TAR PERFORMANCE

The values describing the TAR's performance using each controller were calculated off-line. To calculate the cooling power, the steady-state temperature difference was recorded and averaged over 5 trials. Then, a heat transfer model of the TAR was created in ANSYS. The steady-state temperatures were applied as boundary conditions, and the solver calculated the useful cooling power at the cold end of the stack, $\dot{Q}_{CHX}$. The calculated heat flow at the cold end was then plugged into Equation (65), and the cooling power of the thermoacoustic core, $\dot{Q}_C$, was calculated. The acoustic power applied to the TAR, $\dot{W}$, was calculated from the pressure and acceleration data and averaged. The cooling power and acoustic power then yielded the coefficient of performance of the thermoacoustic core. The Carnot COP (COP_c) was calculated from the temperature difference as $COP_C = 1 - T_c/T_h$, and the coefficient of performance relative to

COP_c (COPR) was found. COPR is the ratio of the actual COP to COP_C, where COP_C is the ideal maximum achievable COP. COPR is often used to quantify the performance of refrigerators. Finally, electrical power input, Π_{elec}, was measured, and the electrothermal coefficient of performance, COP_{elec}, was calculated as the cooling power divided by electrical input power. Note that by definition, the COP does not include any indication of the electroacoustic performance of the driver, whereas the COP_{elec} provides a measure of the overall electrothermal performance of the device.

As seen in Table 3, the PLL performed better than the acoustic pressure gradient ascent control in terms of thermoacoustic efficiency (COP), but the acoustic pressure control resulted in more steady-state cooling power, $\dot{Q}_C$. The maximum acoustic pressure control achieved a temperature difference of 10.32 °C with 7.469 W of acoustic power. Calculations based on these numbers resulted in a cooling power of 16.42 W, which translated into a COP of 2.188 and a COPR of 7.73%. The PLL managed a steady-state cooling power of 10.76 W, a COP of 4.305 and a COPR of 14.19%.

The cooling power was greater under the maximum acoustic pressure control because that controller found the optimum frequency for generating large acoustic pressures in the resonator given a constant amplitude voltage input to the driver. In other words, it tracked the peak of the solid blue curve (near 310 Hz) in the magnitude plot of Figure 28. The increased acoustic pressure translated into increased acoustic power, which resulted in an overall increase in cooling power. On the other hand, the PLL tracked the acoustic resonant frequency, which is the maximum acoustic pressure with respect to a constant amplitude acceleration input to the resonator, or the peak of the dotted green curve (near 295 Hz) in the magnitude plot of Figure 28. This frequency provides the best phase for an efficient thermoacoustic process. However, because the amplitude of the voltage input to the driver was held constant, the acceleration varied with respect to frequency. As a result, less acoustic power was produced by the driver when under PLL control, and in turn, the steady-state cooling power was also lower. However, the ratio of cooling power to acoustic power (COP) was such that the PLL control displayed better thermoacoustic performance.

As the power input to the driver was not constant, it is interesting to compare the controllers' resulting cooling powers with respect to input electrical power. PLL control resulted in 24.76 W of input electrical power and, with the acoustic power shown in Table 3, a COP_{elec} of 0.434. Acoustic pressure gradient ascent control resulted in 28.70 W of input electrical power and a COP_{elec} of 0.572. Relative to COP_C, the electrothermal performances of the TAR under PLL and acoustic pressure control were 1.43% and 2.02%, respectively. Therefore, the acoustic pressure control scheme resulted in a more efficient conversion of electrical power to cooling power under a constant voltage amplitude input to the driver. This makes sense as the PLL control ignores the driver's electrical dynamics whereas the acoustic pressure control operates on a transfer function that involves complete the dynamics of both the driver and the resonator. Therefore, the PLL indirectly controls the thermoacoustic performance of the TAR, whereas the acoustic pressure control indirectly controls the overall electrothermal performance. In the end, the pressure control drew 15.9% more electrical power but resulted in 52.6% more cooling power than the PLL control.

6.0 CONCLUSIONS AND FUTURE WORK

A standing-wave thermoacoustic refrigerator was designed using a dimensionless parameter approach suggested by Tijani [31]. Due to the use of suboptimal parts (i.e. the driver and heat exchanger), and because there was no specific application intended, the final TAR was not comparable to most TARs in literature in terms of cooling power or efficiency; however, there was a notable thermoacoustic effect, which allowed for a comparison of control schemes.

In simulations with a prediction error model, the standard method of control in thermoacoustic applications (a PLL), was compared to two gradient ascent controls, one maximizing acoustic pressure and the other maximizing acoustic power. The PLL displayed the best control characteristics in terms of convergence time and steady-state precision. The acoustic power control appeared to perform comparably to the acoustic pressure control.

Due to difficulties collecting data for the acoustic power control, the PLL was compared quantitatively with only the acoustic pressure control. Again, the PLL performed better in terms of the control criteria (lock-on time and steady-state precision) and thermoacoustic efficiency, but the pressure gradient ascent controller performed better in terms of the cooling power and overall efficiency. In general, the thermodynamic considerations are paramount, but in some niche applications, response time and precision might be of greater importance. That said, convergence time is usually irrelevant as most TAR applications involve continuous operation and slowly changing conditions. Furthermore, the gradient ascent algorithm can be made more precise at the expense of lock-on time, so those controllers could be made more comparable to the PLL in that respect. In fact, a better gradient ascent algorithm could likely be found that would perform better both in terms of lock-on time and precision. The limiting factors to the precision of the gradient ascent approach are measurement noise, which occurs in the PLL as well, and the error of the gradient approximation, which is very small. Overall, the PLL yields better thermoacoustic efficiency, but the pressure gradient ascent control offers better cooling power and better electrothermal efficiency.

Further studies of the acoustic power control are required before conclusions can be drawn regarding its performance, but preliminary results indicate that this method of control is less reliable than either of the other forms of control considered in the present study. Also, it is the most complicated of the schemes, which makes it less desirable.

This study indicates that acoustic pressure gradient ascent control would be better for areas such as electronics cooling, where power density is more important, because it allows more cooling power and involves fewer sensors so that the TAR can be made more compact. Also, with devices that involve manufacturing tolerances, the results discussed above suggest that the acoustic pressure maximizing controller would be best suited due to its higher electrothermal efficiency.

In the future, the next obvious step is to conduct more experiments with the acoustic power controller. Aside from that, it would be interesting to investigate the three controllers on a more precisely designed TAR. The main areas that could be improved are the driver as it was not tuned to match the resonator and the heat exchanger as it failed to reject enough heat to the environment. There is also room for improvement of the resonator in terms of pressurization. Initially, I intended to use helium at 10 atm as the working fluid, but the TAR could not contain the pressure for more than an hour. With a more efficient driver and a better resonator, the effect of the controllers on the overall efficiency of the TAR might be more significant and could be investigated further. Also, a better TAR design would result in a narrower peak in the performance curves used in the gradient ascent algorithm, so the significance of noise in the gradient estimate could be better quantified. All of these things could lead to an overall improvement of thermoacoustic technology by helping to take it one step closer to broad-scale application. Thermoacoustic technology is still relatively young, but it holds much promise for a more sustainable future.

APPENDIX A

MATLAB® CODE

A.1 CODE TO PLOT ROTT'S FUNCTION FOR VARIOUS PORE SHAPES

```
% Plot Rott's function for various pore shapes

clear all

x = linspace(.001,15,1000);     % ratio of hydraulic radius to delta_k
lam = x*2*sqrt(2);              % dimensionless thermal disturbance number
F = zeros(5,length(x));         % initialize F array

% Arnott
y = sqrt(i)*lam;        % intermediate variable
iy = sqrt(-i)*lam;      % intermediate variable

F(1,:) = 1-sqrt(2)./lam*(1+i);                          % boundary layer
F(2,:) = 1-(2./iy).*tanh(iy/2);                         % parallel plates
F(3,:) = 1-(2./y).*(besselj(1,y)./besselj(0,y));        % circular pores
for m=1:2:11                                            % square pores
  for n=1:2:11
    Ymn = 1+i*pi^2./lam.^2*(m^2+n^2)/4;
    F(4,:) = F(4,:) + 64/pi^4./(m^2*n^2*Ymn);
  end
end
F(5,:) = 1-2./(iy).*coth(3*iy/2)+4/3*(i./lam.^2);      % equi. tri. pores

Re = real(1-F);     % f_k = 1 - F (to compare results of Arnott and Swift)
Im = imag(F);       % Im part is same for Arnott and Swift

% Swift
% f_k(1,:) = tanh((1+i)*x) ./ ((1+i)*x);  % parallel plates
% pin array:
  r = 2;                % ratio of pin spacing (cntr-cntr) to pin diameter
  z = (i-1)*x/r;        % for convenience
```

```
  f_pin = -2./(3*z)...
          .*(bessely(1,r*z).*besselj(1,z)-besselj(1,r*z).*bessely(1,z))...
          ./(bessely(1,r*z).*besselj(0,z)-besselj(1,r*z).*bessely(0,z));
Re(6,:) = real(f_pin);
Im(6,:) = imag(f_pin);

figure(),set(gcf,'defaultlinelinewidth',1.5)
plot(x,Re(1,:),'k--',x,Re(2,:),'r:',x,Re(3,:),'g-',...    % plot Re parts
       x,Re(4,:),'m-.',x,Re(5,:),'b:',x,Re(6,:),'c-',...
     x,Im(1,:),'k--',x,Im(2,:),'r:',x,Im(3,:),'g-',...    % plot Im parts
       x,Im(4,:),'m-.',x,Im(5,:),'b:',x,Im(6,:),'c-')
  axis([0 4 -.5 1])
  ylabel('$f_k(r_h/\delta_k)$'), xlabel('$r_h/\delta_k$')
  legend('boundary layer','parallel plate','circular','square',...
           'eq. triangle','pin array')
```

A.2 CODE TO FIND OPERATING FREQUENCY

```
% Find operating frequency based on gas parameters and stack spacing

% Gas properties

  % air @ 20 C, 1 atm
%   K = .0257;          % thermal conductivity (W/m/K)
%   gamma = 1.4;        % ratio of specific heats
%   Cp = 1005;          % isobaric specific heat (J/kg/K)
%   Pr = .713;          % Prandtl number
%   Rs = 286.9;         % specific ideal gas constant

  % He @ 20 C, 1 atm
  K = .138;           % thermal conductivity (W/m/K)
  gamma = 5/3;        % ratio of specific heats
  Cp = 5193.2;        % isobaric specific heat (J/kg/K)
  Pr = .68;           % Prandtl number
  Rs = 2077;          % specific ideal gas constant

% Operating conditions
  Tm = 283.15;        % operating temperature (K)
  pm = 101325;        % operating pressure (Pa)
  rho = pm/Rs/Tm;     % density (kg/m^3)

y = .0011/2;          % half space between stack walls

delta_k = y/.85;      % optimum thermal penetration for square channels
f = K/rho/Cp/delta_k^2/pi;        % optimum operating frequency (Hz)

spc = input('Spacing / delta_k:');
delta_k2 = 2*y/spc;      % spacing / delta_k = 2~4 to not disturb acoustics
f_spc = K/rho/Cp/delta_k2^2/pi;  % operating frequency for 2y = spc*delta_k
```

```
disp(sprintf('\r\rRott frequency (square pores): %0.2f',f))
disp(sprintf('\rFrequency for chosen spacing: %0.2f',f_spc))
```

A.3 CODE TO PLOT POWER CURVES AND COEFFICIENT OF PERFORMANCE FOR VARIOUS STACK LENGTHS AND POSITIONS

```
%TAR  stack design

clear all

% Gas parameters
  % air @ 20 C, 1 atm
%   K = .0257;        % thermal conductivity (W/m/K)
%   gamma = 1.4;      % ratio of specific heats
%   Cp = 1005;        % isobaric specific heat (J/kg/K)
%   Pr = .713;        % Prandtl number
%   Rs = 286.9;       % specific ideal gas constant

  % He @ 20 C, 1 atm
  K = .138;         % thermal conductivity (W/m/K)
  gamma = 5/3;      % ratio of specific heats
  Cp = 5193.2;      % isobaric specific heat (J/kg/K)
  Pr = .68;         % Prandtl number
  Rs = 2077;        % specific ideal gas constant

% Operating parameters
  pm = 101325;          % operating pressure (Pa)
  Tm = 280.15;          % mean temperature (K)
  deltaT = 30;          % desired temperature difference (K)
  freq = 365;           % resonant frequency (Hz)

  rho = pm/Rs/Tm;             % density (kg/m^3)
  c = sqrt(gamma*Rs*Tm);      % speed of sound (m/s)
  deltaTn = deltaT/Tm;        % normalized temp. difference
  w = 2*pi*freq;              % resonant frequency (rad/s)
  lambda = c/freq;            % wavelength (m)
  k = w/c;                    % wave number

% Driver parameters
  D = .01;          % drive ratio (po/pm)

% Stack Parameters
  y0 = .00110/2;                        % half pore diameter (m)
  l = .00020/2;                         % half wall thickness (m)
  delta_k = sqrt(2*K/(rho*Cp*w));       % thermal penetration (m)
  delta_kn = delta_k/y0;                % normalized therm. penetration
  A = pi*(.0508)^2;                     % area of resonator at stack (m^2)
  B = y0^2/(y0+l)^2;                    % "blockage factor" for square pores
```

```
% Choose lengths and position range of interest
  L = .0254*[1.5 2 2.5 3 3.5];       % stack lengths (in. -> m)
    for i=1:length(L)                % create strings for legend
      Lstr{i} = [num2str(L(i),'%0.3f') ' m'];
    end
  x = linspace(0,.25,1001);          % stack center position (m)
  Ln = L*k;                          % norm. stack length
  xn = x*k;                          % norm. stack position (x*k)

% Initialize vectors
  Qcn = zeros(1,1001);  % normalized cooling power
  Wn = zeros(1,1001);   % normalized acoustic power

% Calculate normalized performance
  for i=1:1:length(Ln)

    % intermediate variables
      Lambda = 1-sqrt(Pr)*delta_kn+.5*Pr*delta_kn^2;
      Gamma = deltaTn./((gamma-1)*B*Ln(i))*tan(xn);

    Qcn(i,:) = -((delta_kn*D^2*sin(2*xn)/(8*gamma*(1+Pr)*Lambda))...
      .*((Gamma*(1+sqrt(Pr)+Pr)/(1+sqrt(Pr)))...
      -(1+sqrt(Pr)-sqrt(Pr)*delta_kn)));

    Wn(i,:) = -(delta_kn*Ln(i)*D^2*(gamma-1)*B*cos(xn).^2/(4*gamma) ...
      .*((Gamma/((1+sqrt(Pr))*Lambda))-1)...
      -delta_kn*Ln(i)*D^2*sqrt(Pr)*sin(xn).^2/(4*gamma*B*Lambda));

  end

  COP = Qcn./Wn;         % coefficent of performance

% Evaluate parameters based on operating conditions
  Qc = Qcn*pm*c*A;       % cooling power (W)
  W = Wn*pm*c*A;         % acoustic power (W)
  L = Ln/k;              % stack length (m)
  x = xn/k;              % stack center position (m)

set(0,'defaulttextinterpreter','latex')
figure(1),set(gcf,'defaultlinelinewidth',1.5)
  plot(x,COP)
  axis([0 .25 0 5])
  xlabel('Stack Center Position (m)'),ylabel('COP')
  legend(Lstr), grid on
figure(2),set(gcf,'defaultlinelinewidth',1.5)
  plot(x,Qc)
  axis([0 .25 0 2])
  xlabel('Stack Center Position (m)'),ylabel('$Q_c (W)$')
  legend(Lstr), grid on
figure(3),set(gcf,'defaultlinelinewidth',1.5)
  plot(x,W)
  axis([0 .25 0 1.5])
  xlabel('Stack Center Position (m)'),ylabel('W (W)')
  legend(Lstr), grid on
```

A.4 CODE TO CALCULATE AND PLOT GRADIENT ERROR

```
set(0,'defaulttextinterpreter','latex')

load HE1.vna -mat
range = 961:1121;        %full:(1:1601) p_max:(897:1089), P_max:(961:1121)
f = SLm.fdxvec(range)';
p = SLm.xcmeas(1,2).xfer(range)*339.91;
a = SLm.xcmeas(1,3).xfer(range)*460.68;
v = a./(1i*f);
P = .5*real(p.*conj(v));
[c S mu] = polyfit(f,P,5);        %prms: abs(p)*sqrt(2)/2
C = polyval(c,f,[],mu);
figure()
  plot(f,P,f,C)

dw = .1:.1:5;
E = zeros(length(f),50);
for i = 1:length(f)
  w1 = f(i);
  w1hat = (w1-mu(1))/mu(2);
  for j = 1:length(dw)
    w2hat = w1hat+dw(j)/mu(2);
    E(i,j) = -(taylor(c,w1hat,w2hat,5)-taylor(c,w1hat,w2hat,1))/mu(2);
  end
end
Etrunc = mean(abs(E),1);
Emeas = 2*.0073./dw;

figure()
  plot(dw,Etrunc,dw,Emeas,'--',dw,Etrunc+Emeas,':')
    ylabel('Approximate Error $$\left(\frac{Pa}{rad/s}\right)$$')
    xlabel('$$\Delta\omega$$ $$(rad/s)$$'),axis([2 5 0 2e-4])
    legend('$$E_{trunc}$$','$$E_{meas}$$','$$E_{tot}$$')
```

APPENDIX B

MODELS

B.1 IDENTIFIED MODEL OF TAR

$$
\begin{aligned}
\dot{x} &= Ax + Bu + Ke(t) \\
y &= Cx + Du + e(t)
\end{aligned}
$$

where

$$
\mathbf{A} = \begin{bmatrix}
-258.16 & 893.32 & 140.77 & -1175.6 & 796.37 & -62.106 & 857.09 & 74.696 & 307.4 & 502.04 \\
-752.41 & -76.348 & 1452.4 & -21.043 & -133.69 & -16.684 & -342.02 & 121.11 & -201.5 & -169.13 \\
-424.57 & -1510.8 & -246.82 & -1439.2 & 521.19 & -146.56 & 329 & 374.6 & 383.19 & 213.84 \\
731.54 & 183 & 1123.8 & -308.04 & 567.23 & -114.93 & 1110.2 & 146.97 & 298.15 & 520.41 \\
-90.875 & -41.128 & -137.24 & 125.93 & -582.57 & 397.36 & -2526.2 & -331 & -475.5 & -735.16 \\
-19.872 & -5.2926 & -18.905 & 27.441 & -308.62 & -58.363 & -203.41 & 120.3 & 157.15 & 84.974 \\
56.742 & 38.71 & 88.378 & -137.07 & 1231.2 & 320.17 & -991.07 & 575.51 & -1609 & -1302 \\
-18.933 & 1.6994 & -8.2503 & -105.89 & 281.62 & 45.602 & -623.52 & -305.27 & -2509.7 & -254.27 \\
-9.6394 & -12.339 & 17.472 & 17.011 & -193.94 & -82.939 & 779.48 & 2372.7 & 110.17 & -340.56 \\
106.6 & -18.706 & 42.805 & -24.131 & -280.3 & -83.817 & 514.89 & 469.21 & -56.057 & -959.09
\end{bmatrix}
$$

$$
\mathbf{B} = \begin{bmatrix} 486.47 & -526.9 & 1240.5 & 3407 & -1080.9 & -118.52 & 314.28 & -687.08 & -395.21 & -941.94 \end{bmatrix}^T
$$

$$
\mathbf{C} = \begin{bmatrix}
-3.252 & 8.543 & 15.867 & -1.5316 & 5.002 & 10.26 & 13.054 & -18.432 & -4.4668 & 15.1 \\
25.634 & -3.8704 & 18.554 & 34.373 & -42.938 & 9.2864 & -61.105 & 14.709 & 3.0098 & -44.389
\end{bmatrix}
$$

$$
\mathbf{D} = \begin{bmatrix} 0 \\ 0 \end{bmatrix}
$$

$$
K = \begin{bmatrix}
0 & 0 & 0 & 0 & 0 & 0 & 0 & 0 & 0 & 0 \\
0 & 0 & 0 & 0 & 0 & 0 & 0 & 0 & 0 & 0
\end{bmatrix}^T
$$

B.2 SIMULINK™ SCHEMATICS

B.2.1 PLL Simulation

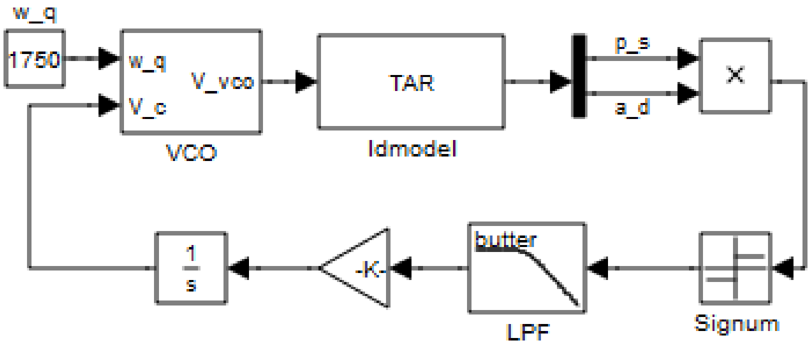

B.2.2 Acoustic Pressure Gradient Ascent Simulation

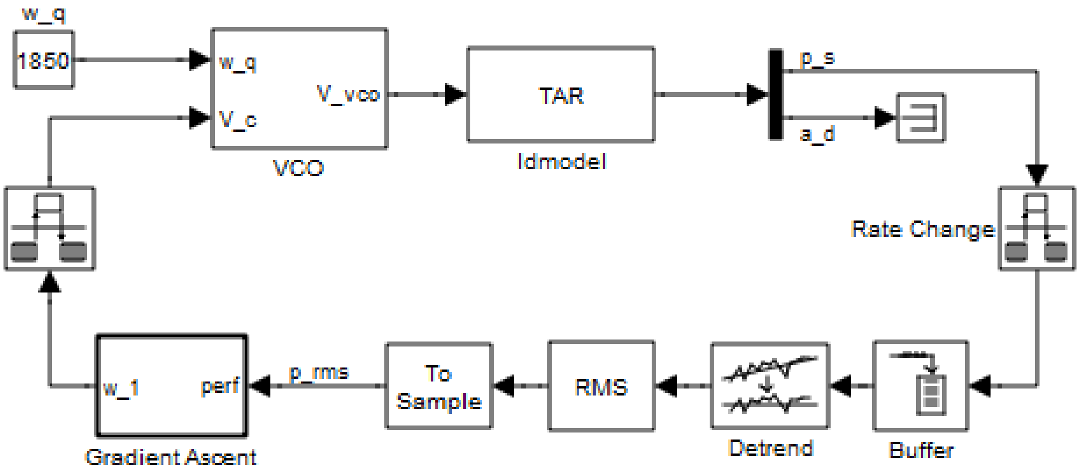

B.2.3 Acoustic Power Gradient Ascent Simulation

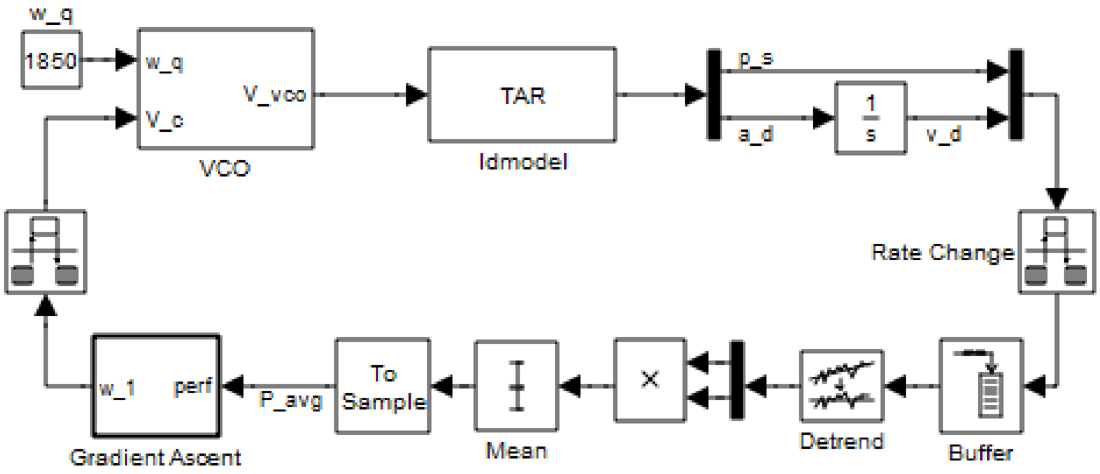

BIBLIOGRAPHY

[1] Putnam AA, Dennis WR, 1956, "Survey of organ-pipe oscillations in combustion systems," J Acoust Soc Am, **28** (2), pp. 246-259.

[2] Higgins B, 1802, Nicholson's J **1**, p. 130.

[3] Rijke PL, 1859, "Notiz über eine neue Art, die in einer an beiden enden offenen Röhre enthaltene Luft in Schwingungen zu versetzen," Ann Phys **107** (6), pp. 339-43.

[4] Feldman KT, Jr., 1968, "Review of the literature on Rijke thermoacoustic phenomena," J Sound Vib **7** (1), pp. 83-9.

[5] Bisio G, Rubatto G, 1999, "Sondhauss and Rijke oscillations—thermodynamic analysis, possible applications and analogies," Energy **24**, pp. 117-131.

[6] Sondhauss C, 1850, "Ueber die Schallschwingungen der Luft in erhitzten Glasröhren und in gedeckten Pfeifen von ungleicher Weite, "Ann Phys Chem **79**, pp. 1-34.

[7] Feldman KT, Jr., 1968, "Review of the literature on Sondhauss thermoacoustic phenomena," J Sound Vib **7** (1), pp. 71-82.

[8] Taconis KW, Beenakker JJM, Nier AOC, Aldrich LT, 1949, "Measurements concerning the vapor-liquid equilibrium of solutions of He^3 in He^4 below 2.19°K," Physica **15** (8-9), pp. 733-9.

[9] Yazaki T, Tominaga A, Narahara Y, 1980, "Experiments on thermally driven acoustic oscillations of gaseous helium," J Low Temp Phys **41** (1-2), pp. 45-60.

[10] Lord Rayleigh (Strutt JW), 1945, *The Theory of Sound,* Dover, New York, 2nd ed.

[11] Kirchhoff G, 1868, "Ueber den Einfluss der Wärmeleitung in einem Gase auf die Schallbewegung," Ann Phys **134** (6), pp. 177-93

[12] Kramers HA, 1949, "Vibrations of a gas column," Physica **15** (11-12), pp. 971-84.

[13] Rott N, 1969, "Damped and thermally driven acoustic oscillations in wide and narrow tubes," Z angew Math Phys **20**, pp. 230-43.

[14] Rott N, 1973, "Thermally driven acoustic oscillations. Part II: stability limit for helium," Z angew Math Phys **24**, pp. 54-73.

[15] Rott N, 1975, “Thermally driven acoustic oscillations. Part III: second-order heat flux,” Z angew Math Phys **26**, pp. 43-49.

[16] Rott N, 1976, “Thermally driven acoustic oscillations. Part IV: tubes with variable cross-section,” Z angew Math Phys **27**, pp. 197-224.

[17] Rott N, 1983, “Thermally driven acoustic oscillations. Part VI: excitation and power,” Z angew Math Phys **34**, pp. 609-26.

[18] Swift GW, 1997, “Thermoacoustic engines and refrigerators,” Encyclopedia Appl Phys, **21**, pp. 245-64.

[19] Wheatly JC, Hofler TJ, Swift GW, Migliori A, 1985, “Understanding some simple phenomena in thermoacoustics with applications to acoustical heat engines,” Am J Phys, **53**, pp. 147-62.

[20] Swift GW, 1988, “Thermoacoustic engines,” J Acoust Soc Am, **84**, pp. 1146-80.

[21] Wheatley JC, Hofler T, Swift GW, Migliori A, 1983, “Experiments with an intrinsically irreversible thermoacoustic heat engine,” Phys Rev Lett **50** (7), pp.499-502.

[22] Hofler TJ, 1986, “Thermoacoustic refrigerator design and performance,” Ph.D. dissertation, University of California at San Diego.

[23] Tijani MEH, Zeegers JCH, de Waele ATAM, 2002, “Construction and performance of a thermoacoustic refrigerator,” Cryogenics, **42**, pp. 59-66.

[24] Garrett SL, Adeff JA, Hofler TJ, 1993, “Thermoacoustic refrigerator for space applications,” J Thermophys Heat Transfer, **7**, pp. 595-99.

[25] Swift GW, 1992, “Analysis and performance of a large thermoacoustic engine,” J Acoust Soc Am **92** (3), pp. 1551-63.

[26] Ballister SC, McKelvey DJ, 1995, “Shipboard electronics thermoacoustic cooler,” M.S. thesis, Naval Postgraduate School, Monterey, CA.

[27] Backhaus S, Swift GW, 2000, “A thermoacoustic-Sterling heat engine: Detailed study,” J Acoust Soc Am **107** (6), pp. 3148-66.

[28] Adeff JA, Hofler TJ, 2000, “Design and construction of a solar-powered, thermoacoustically driven, thermoacoustic refrigerator,” J Acoust Soc Am **107** (6), pp. L37-L42.

[29] Arnott WP, Bass HE, Raspet R, 1991, “General formulation of thermoacoustic for stacks having arbitrarily shaped pore cross sections,” J Acoust Soc Am, **90** (6), pp. 3228-37.

[30] Tijani MEH, Zeegers JCH, de Waele ATAM, 2002, “Prandtl number and thermoacoustic refrigerators,” J Acoust Soc Am, **112** (1), pp. 134-43.

[31] Tijani MEH, Zeegers JCH, de Waele ATAM, 2002, "Design of thermoacoustic refrigerators," Cryogenics, **42**, pp. 49-57.

[32] Tijani MEH, Zeegers JCH, de Waele ATAM, 2002, "The optimal stack spacing for thermoacoustic refrigeration," J Acoust Soc Am, **112** (1), pp. 128-33.

[33] Swift GW, Keolian RM, 1993, "Thermoacoustics in pin-array stacks," J Acoust Soc Am, **94** (2), pp. 941-3.

[34] Swift GW, 1995, "Thermoacoustic engines and refrigerators," Physics Today, **48** (7), pp. 22-8.

[35] Olson JR, Swift GW, 1994, "Similitude in thermoacoustics," J Acoust Soc Am, **95** (3), pp. 1405-12.

[36] Belcher JR, Slaton WV, Raspet R, Bass HE, Lightfoot J, 1999, "Working gases in thermoacoustic engines," J Acoust Soc Am, **105** (5), pp. 2677-84.

[37] Ward B, Clark J, Swift G, 2008, "Design Environment for Low-amplitude Thermoacoustic Energy Conversion," Version 6.2, Los Alamos National Laboratory. Available from: www.lanl.gov/thermoacoustics/DeltaEC.html.

[38] Herman C, Travnicek Z, 2005, "Cool sound: the future of refrigeration? Thermodynamic and heat transfer issues in thermoacoustic refrigeration," Heat and Mass Transfer **42**, pp. 492-500.

[39] Li Y, Chiu GT-C, Mongeau LG, 2002, "Dual-driver standing wave tube: acoustic impedance matching with robust repetitive control," Proc Amer Control Conf.

[40] Kinsler LE, Frey AR, Coppens AB, Sanders JV, 1982, *Fundamentals of Acoustics*, John Wiley & Sons, Inc., New York, 3rd ed.

[41] Fox RW, McDonald AT, Pritchard PJ, 2004, *Introduction to Fluid Mechanics*, John Wiley & Sons, Inc., 6th ed.

[42] Fan L, Zhang SY, Wang BR, 2006, "Coupling between thermoacoustic resonance pipes and piezoelectric loudspeakers studied by equivalent circuit method," J Acoust Soc Am, **120** (3), pp. 1381-7.

[43] Wakeland RS, 2000, "Use of electrodynamic drivers in thermoacoustic refrigerators," J Acoust Soc Am, **107** (2), pp. 827-32.

[44] Li Y, Rotea M, Chiu GT-C, Mongeau LG, 2005, "Extremum seeking control of a tunable thermoacoustic cooler," IEEE Trans Control Syst Technol, **13** (4), pp. 527-36.

[45] Shearer TL, Hofmann HF, Smith RWM, Garrett SL, 2004, "Sensorless control of a thermoacoustic refrigerator," J Acoust Soc Am, **116** (1), pp. 288-93.

[46] Banerjee D, 2006, *PLL Performance, Simulation, and Design*, Dog Ear Publishing, LLC., 4th ed.

[47] Swift GW, 2009 (private communication via e-mail).

[48] Widrow B, Stearns SD, 1985, *Adaptive Signal Processing*, Prentice-Hall, Inc., Englewood Cliffs, NJ.

[49] Norton MP, Karczub DG, 2003, *Fundamentals of Noise and Vibration Analysis for Engineers*, Cambridge University Press, 2nd ed.

[50] Smith AK, 2005, "Adaptive Resonant Mode Active Noise Control," M.S. thesis, University of Pittsburgh.

[51] Dickason V, 1997, *The Loud Speaker Design Cookbook*, Audio Amateur Press, Peterborough, NH.